

Chapter 12

Laser Satellite Communication Systems

12.1	Introduction	478
12.2	Atmospheric Channels	479
12.2.1	Optical turbulence profiles	480
12.2.2	Outer scale models	483
12.3	Background	484
12.3.1	Satellite orbits	484
12.3.2	Past studies	485
12.3.3	Pointing and tracking	488
12.3.4	Optical wave models	488
12.4	Second-Order Statistics	490
12.4.1	Spatial coherence radius	491
12.4.2	Angle-of-arrival fluctuations	492
12.4.3	Isoplanatic angle	493
12.5	Irradiance Statistics: Downlink Channel	493
12.5.1	Mean irradiance	494
12.5.2	Scintillation index	495
12.5.3	Covariance function of irradiance	498
12.6	Irradiance Statistics: Uplink Channel	500
12.6.1	Mean irradiance	500
12.6.2	Beam wander	501
12.6.3	Scintillation index	502
12.6.4	Strong fluctuation theory	506
12.6.5	Covariance function of irradiance	509
12.7	Fade Statistics: Downlink Channels	510
12.7.1	Fractional fade time	511
12.7.2	Expected number of fades	513
12.7.3	Mean fade time	515
12.8	Fade Statistics: Uplink Channels	516
12.8.1	Gamma-gamma distribution	516
12.8.2	Fractional fade time	518
12.8.3	Expected number of fades	519
12.8.4	Mean fade time	520
12.9	Summary and Discussion	520
12.10	Worked Examples	524
	Problems	526
	References	529

Overview: In this chapter we consider statistical quantities introduced in Chaps. 6–9 and adapt them to vertical and slant path propagation links. Most of the analysis presented here is for a slant path connecting a satellite in geostationary orbit and a ground or airborne platform. The uplink and downlink paths for such links are vastly different because the atmospheric turbulence layer is only near the transmitter on an uplink path and only near the receiver on a downlink path. This difference in path for the two cases leads to important differences in the derived expressions for *beam spreading*, *scintillation index*, *spatial coherence radius* of the wave, and the effect these parameters have on the *probability of fade*. In particular, we examine the effect that beam wander has on the scintillation index of an uplink path to space and its implications on fading statistics.

The greatest difference in modeling uplink/downlink paths (or general slant paths) compared with horizontal propagation paths is that in the former we need to consider changes in the refractive index structure parameter C_n^2 along the path. Generally, changes in C_n^2 along the path can be inferred from a profile model of C_n^2 as a function of altitude. In our work here we rely on the *Hufnagle-Valley C_n^2 profile model*, but this is not essential for the general analysis. We choose this model because it offers a little more generality than other C_n^2 profile models through the use of two independent parameters identifying ground-level C_n^2 values and upper atmospheric wind speeds.

Weak fluctuation theory based on the Rytov approximation is sufficient for most of the calculations required in the analysis of an uplink or downlink path provided the zenith angle is sufficiently small (less than 60 deg in most cases but may be restricted to zenith angles less than 45 deg in cases where ground-level C_n^2 is large). However, it may be necessary to use strong fluctuation models for large-diameter beams in the presence of beam wander effects, and/or large zenith angles such as those that occur in near-horizon propagation paths.

12.1 Introduction

The possibility of using high-data-rate optical transmitters for satellite communication channels has generated interest over three decades in laser communication systems for ground/airborne-to-space and space-to-ground/airborne data links. The future for laser satellite communications (called *laser satcom*) at optical frequencies depends primarily on its ability to provide distinct advantages as compared with microwave systems. The major advantages of an optical wave system over a conventional *radio frequency* (RF) system are consequences of the short wavelengths associated with optical waves. Although given in Chapter 11, we repeat them below [1]:

1. smaller antenna (telescope);
2. less mass, power, and volume; i.e., optical wave systems have approximately one-third the mass of microwave systems, consume one-half or less the prime power of microwave systems, occupy one-third to one-tenth the volume of microwave systems;
3. intrinsic narrow-beam and high-gain nature of lasers, i.e., laser satcom systems have ~ 60 dB more gain (can be used to raise data rate), the system's narrow beams are basically immune to jamming and interception/detection by adverse parties; narrow beams preclude signal interference that currently limits the number of satellites using microwave frequencies within the allocated spectrum;
4. no regulatory restrictions for frequency use and bandwidths; which permit very high data rates, virtually unconstrained by carrier frequency.

Some historical background on past and recent laser satcom programs in the United States and abroad was provided in Section 1.4.1. In addition to technology developments, there have been a number of studies concerning optical scintillations and fade statistics associated with both uplink and downlink satellite communication channels (Section 12.3.2). Although most of the early analyses involved either spherical waves or on-axis Gaussian-beam waves, more recent studies and experimental data of scintillations associated with Gaussian-beam waves have revealed that scintillation levels increase with the square of distance from the (nominal) optical axis, eventually resulting in a radial saturation effect [2–5]. Such increases in scintillation level with radial distance have significant negative impact on the fade statistics as a result of pointing errors [4]. Even on downlink channels for which the scintillations are basically uniform across the beam spot size, pointing errors have negative impact on the fade statistics owing to the Gaussian shape of the mean irradiance profile.

The numerical results presented in this chapter are based on the Hufnagel-Valley atmospheric model (Section 12.2.1) and the special case of a satellite in geosynchronous orbit or low Earth orbit. However, all theoretical expressions are valid for other atmospheric models and other laser communication links.

12.2 Atmospheric Channels

The atmosphere is composed of a collection of gases, atoms, water vapor, and various chemical particulates that are trapped by the Earth's gravitational field. Consisting of several distinct layers (recall Section 1.3), the atmosphere extends to approximately 700 km, or 400 miles, above the Earth's surface with the heaviest concentration of particles in the first 20 km above the surface. Electromagnetic waves passing through the atmosphere suffer power losses and wave front distortions caused by absorption and scattering of the radiation by the various particulates. These effects are most severe as the wavelength of the wave approaches the size of the particles, typically on the order of centimeters down to micrometers.

Atmospheric conditions can be roughly classified as (i) clear air, (ii) clouds, and (iii) rain and fog. Here, we are concerned only with *clear-air turbulence*, which is more benign and characterized by long-range visibility and relatively low attenuation. As discussed in Chap. 3, the primary consideration for optical/IR waves propagating in clear-air turbulence is the presence of temperature gradients that produce changes in the index of refraction (i.e., *optical turbulence*), causing turbulent eddies to act as random optical lenses.

The *atmospheric boundary layer* (ABL) is the region close to the Earth where atmospheric dynamics are dominated by the interaction and heat exchange with the Earth's surface. In the daytime, the ABL extends to roughly 1 to 2 km above the surface. Numerous measurements of the refractive-index structure parameter C_n^2 (or, equivalently, the temperature structure parameter C_T^2) have been made near the Earth's surface over land and water using point measurements on towers, path measurements between various locations, and probes on aircraft. During the day the sun heats the ground, creating unstable conditions due to layers of cold air above the warm ground. This convective instability gives rise to thermal plumes and strong optical turbulence. Daytime measurements of C_n^2 reveal that optical turbulence is strongest near the ground with typical values of 10^{-13} or $10^{-14} \text{ m}^{-2/3}$. With increasing altitude h above a uniform terrain, values of C_n^2 normally decrease at a rate of approximately $h^{-4/3}$. This classic behavior in C_n^2 is observed during conditions when convection dominates the boundary layer dynamics. Above a complex terrain like a mountainous area, a less steep slope of roughly $h^{-1/3}$ has been observed [6]. At night, warmer air over colder ground creates more stable conditions and a decrease of C_n^2 with altitude at a rate of approximately $h^{-2/3}$. Thermally neutral conditions usually occur around sunrise and sunset when the surface and air temperatures are nearly identical, resulting in very low wind speed and minimum values of C_n^2 over short periods of time. These low values of C_n^2 occur because of an absence of temperature gradients.

Above the ABL up to roughly 40 km is the *free atmosphere*, which consists of the troposphere, tropopause region, and stratosphere. Upper atmosphere optical turbulence has been measured by thermal probes on balloons and aircraft, stellar scintillation, and radar (e.g., see [27–41] in Chap. 3). Optical turbulence is not well understood in these regions, but the general characteristic of C_n^2 in the free atmosphere is stratification superimposed on an exponential falloff. Although standard atmospheric spectral models are based on isotropic conditions throughout the boundary layer and free atmosphere, evidence now exists that turbulence in the stratosphere is nonisotropic [7,8].

12.2.1 Optical turbulence profiles

For applications involving propagation along a horizontal path, it is customary to assume the structure parameter C_n^2 remains essentially constant (see Chap. 11). Propagation along a vertical or slant path, however, requires a $C_n^2(h)$ profile model to describe properly the varying strength of optical turbulence as a function

of altitude h . Several $C_n^2(h)$ profile models, including both day and night models, are used by the technical community for ground-to-space or space-to-ground applications [9]. One of the most widely used models is the Hufnagel-Valley (H-V) model described by

$$C_n^2(h) = 0.00594(w/27)^2(10^{-5}h)^{10} \exp(-h/1000) \\ + 2.7 \times 10^{-16} \exp(-h/1500) + A \exp(-h/100), \quad (1)$$

where h is in meters [m], w is the rms windspeed (pseudowind) in meters per second [m/s], and A is a nominal value of $C_n^2(0)$ at the ground in $\text{m}^{-2/3}$.

The rms windspeed in (1) is determined from

$$w = \left[\frac{1}{15 \times 10^3} \int_{5 \times 10^3}^{20 \times 10^3} V^2(h) dh \right]^{1/2}, \quad (2)$$

where $V(h)$ is often described by the Bufton wind model, which we write as

$$V(h) = \omega_s h + V_g + 30 \exp \left[- \left(\frac{h - 9400}{4800} \right)^2 \right]. \quad (3)$$

The quantity V_g is the ground wind speed and ω_s is the *slew rate* associated with a satellite moving with respect to an observer on the ground. The slew rate becomes important in making temporal calculations.

Permitting variations in high-altitude wind speed and local near-ground turbulence conditions makes the H-V profile model attractive for theoretical studies. In our calculations, we use the H-V model with $w = 21$ m/s and $A = 1.7 \times 10^{-14} \text{m}^{-2/3}$, commonly known as the H-V_{5/7} model. That is, for wavelength $\lambda = 0.5 \mu\text{m}$, a value of 5 cm is calculated for the atmospheric coherence diameter (Section 6.5.1) and a value of 7 μrad for the isoplanatic angle (Section 12.4.3) for a receiver at the ground looking up. To illustrate the effect on the general H-V model of changing these parameters, three values of moderate to strong wind speed ($w = 10, 21$, and 30 m/s) and two values of nominal ground turbulence levels ($A = 1.7 \times 10^{-14}$ and $A = 1.7 \times 10^{-13} \text{m}^{-2/3}$) are shown in Fig. 12.1. We can see that the ground turbulence level has little effect above 1 km and the wind speed governs the profile behavior primarily in the vicinity of 10 km.

Although site dependent, other C_n^2 models regularly used are the so-called SLC day and night models. The acronym SLC stands for *submarine laser communication* studies. The SLC day model, based on daytime averages of the Miller-Zieske profile [10], is defined by

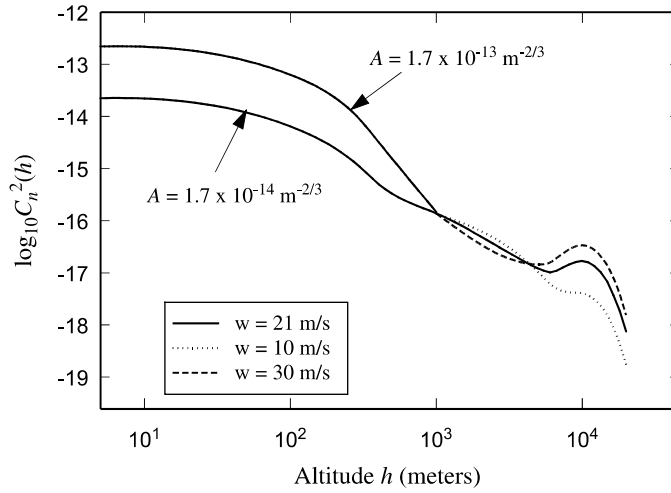


Figure 12.1 $C_n^2(h)$ profile associated with the H-V day model as a function of altitude h . Values of A represent C_n^2 near ground level whereas w denotes high-altitude wind speed.

$$\begin{aligned}
 \text{SLC day model: } C_n^2(h) &= 1.7 \times 10^{-14}, & 0 < h < 18.5 \text{ m}, \\
 &= 3.13 \times 10^{-13}/h^{1.05}, & 18.5 < h < 240 \text{ m}, \\
 &= 1.3 \times 10^{-15}, & 240 < h < 880 \text{ m}, \\
 &= 8.87 \times 10^{-7}/h^3, & 880 < h < 7200 \text{ m}, \\
 &= 2.0 \times 10^{-16}/h^{1/2}, & 7200 < h < 20000 \text{ m}.
 \end{aligned} \tag{4}$$

The corresponding SLC night model, which differs from the daytime model only below altitudes of 1.5 km, is given by

$$\begin{aligned}
 \text{SLC night model: } C_n^2(h) &= 8.4 \times 10^{-15}, & 0 < h < 18.5 \text{ m}, \\
 &= 2.87 \times 10^{-12}/h^2, & 18.5 < h < 110 \text{ m}, \\
 &= 2.5 \times 10^{-16}, & 110 < h < 1500 \text{ m}, \\
 &= 8.87 \times 10^{-7}/h^3, & 1500 < h < 7200 \text{ m}, \\
 &= 2.0 \times 10^{-16}/h^{1/2}, & 7200 < h < 20000 \text{ m}.
 \end{aligned} \tag{5}$$

These particular SLC models represent median values of C_n^2 above the Air Force Maui Optical Station (AMOS) on Mt. Haleakala, Maui, Hawaii, and therefore may not be very representative of other geographical locations. Additional detail and other C_n^2 profile models can be found in Beland [9].

12.2.2 Outer scale models

It is widely accepted that the power spectrum of refractive-index fluctuations does not assume a universal form in the energy range defined by wave numbers $\kappa < 1/L_0$, where L_0 is the outer scale. That is, the shape of the spectrum in this regime at low altitudes must depend largely on the topography of the Earth's surface and local meteorological conditions. Therefore, the assumption of homogeneity and isotropy of the turbulence is no longer valid. Nonetheless, it is still useful to develop simple and convenient models of the spectrum for the low-wave-number regime. Spectrum models that satisfy this criteria are the *von Kármán spectrum* and the *modified atmospheric spectrum* [Eqs. (20) and (22) in Chap. 3]. It is understood that such models only describe some approximate behavior of the spectrum in the low-wave-number range. The primary features of such models are that they reduce to the Kolmogorov spectrum within the inertial subrange $1/L_0 \ll \kappa \ll 1/l_0$ and that

$$\int_0^\infty \kappa \Phi_n(\kappa) d\kappa < \infty.$$

Neither the Kolmogorov nor Tatarskii spectrum satisfy this last condition, which is related to the random phase variance of an optical wave in the geometrical optics approximation (see Section 8.6).

Information about behavior of the outer scale as a function of altitude h is not conclusive. Near the ground it is often assumed that $L_0 \sim 0.4h$, or $L_0 \sim 0.5h$, which, if used at higher altitudes, would lead to predictions of outer scale as large as tens of meters in relatively low altitudes. On the other hand, measurements based on scintillation detection and ranging (SCIDAR) observations in France and in the United States suggest that the outer scale changes with altitude according to the empirical formula [11]

$$L_0(h) = \frac{4}{1 + \left(\frac{h - 8500}{2500}\right)^2}, \quad (6)$$

which limits the outer scale to 4 m or less. Additional SCIDAR observations at the European Southern Observatory in Chile led to a similar model described by [11]

$$L_0(h) = \frac{5}{1 + \left(\frac{h - 7500}{2500}\right)^2}. \quad (7)$$

In this latter case, the outer scale is restricted to 5 m or less. Although Coulman et al. [11] claim validity of these formulas above 2 km, Tatarskii and Zavorotny [12] have suggested that models (6) and (7) are valid only in the surface-layer turbulence.

More recent measurements [13,14] of the parameters of homogeneous, isotropic turbulence in the upper atmosphere led to outer scale values in the

range $5 \leq L_0 \leq 190$ m and varying values of the spectral index α from $11/6$ for the von Kármán spectrum in the range $1.52 \leq \alpha \leq 1.73$. No estimates of inner scale were obtained.

12.3 Background

In this section we review the types of orbits used for satellites, previous studies of uplink/downlink propagation to and from satellites, and introduce the notion of pointing and tracking necessary for moving platforms.

12.3.1 Satellite orbits

There are several basic orbits that are commonly used in satellite communication systems. The earliest communications satellites used the *low Earth orbit* (LEO) primarily because of limitations in launch vehicle capabilities. LEOs, usually at altitudes of several hundred to several thousand kilometers, are still used by the military and NASA (the International Space Station is a LEO satellite and the Space Shuttle flies in a LEO), among others. The period of a LEO is ~ 90 min.

The *geostationary Earth orbit* (GEO) is the one used today by almost all communication relay satellites and meteorological satellites (see Fig. 12.2). In this special circular equatorial orbit at an altitude that varies between 35,786 and 41,680 km, the period of a satellite is exactly equal to the rotation of the Earth. Thus, a GEO satellite appears stationary in the sky when viewed from the ground. If the inclination angle of the orbit with the equator is not zero, but the satellite motion is synchronized with the Earth's 24 h period, the orbit is called a *geosynchronous orbit*.

To provide northern polar coverage, Russian satellites often use a special elliptical orbit called a *Molniya* orbit (see Fig. 12.3). This is a 12 h orbit inclined about 65° to the equator that varies in altitude from 40,000 km (apogee) to approximately 500 km (perigee). It takes at least three or four satellites in this orbit to provide continuous service to Russia because each can be used only 6–8 h during a 24 h period.

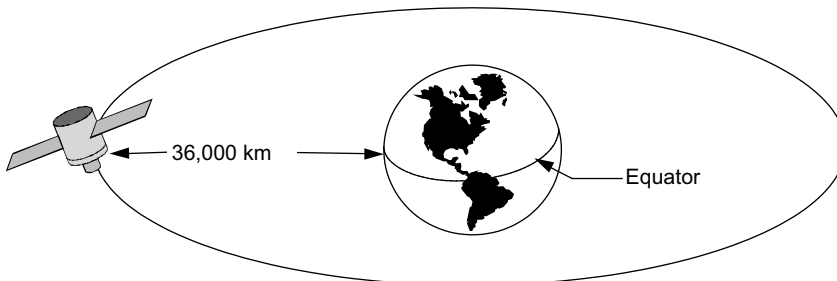


Figure 12.2 Geostationary orbit.

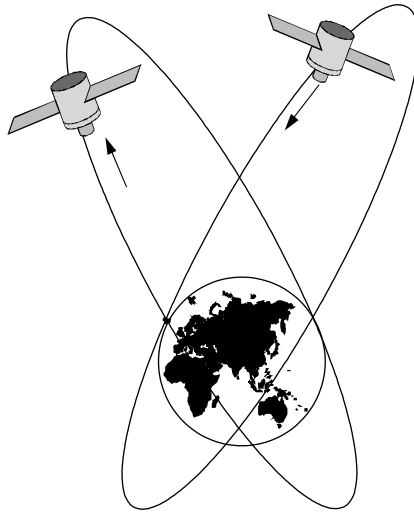


Figure 12.3 Molniya orbits.

Although space laser communication systems will never completely replace RF systems, there are a number of applications for which laser satcom is well suited. These include satellite crosslinks and some communication links between satellites and ground stations. Satellite crosslinks are communication links in space that include LEO to LEO, LEO to GEO, and GEO to GEO. By ground station, we include land-fixed, land-mobile, shipborne, submarine, and airborne stations. Because of crowded frequency assignments and the fact that RF systems cannot transmit very high data rates from geosynchronous orbit, a satellite-to-ground link may prove to be an excellent application for future laser communications.

12.3.2 Past studies

One of the first theoretical studies of scintillation for an uplink communications path was done in the mid-1960s by Fried [15] who used weak fluctuation theory and a collimated Gaussian-beam model. Fried concluded that a substantial reduction in on-axis scintillation occurs with larger beams. A few years later Minott [16] discussed experimental data obtained in 1968 from a continuous wave (CW) argon laser ($0.488\ \mu\text{m}$) beamed at a GEOS-II satellite orbiting at approximately 1250 km. Including zenith angles up to 45° , the experimental data were in reasonable agreement with a lognormal model for the normalized variance (scintillation index), power spectral density, and probability distribution of the scintillations. Titterton [17] did a study similar to Fried's [15] that included focused and defocused beams and concluded that even greater reductions in on-axis scintillation could be achieved with focused beams. However, this conclusion is not supported by experimental data.

Bufton et al. [18] developed a theoretical model in the mid-1970s for a ground-to-space-to-ground retroreflector configuration of satellite laser ranging. For the uplink path, conventional weak fluctuation theory was proposed based on a spherical wave optical model and lognormal probability distribution for the intensity. Speckle statistics associated with the retroreflector array were assumed to be governed by the gamma distribution. A probability distribution model combining lognormal and gamma statistics was the principal result of this study. In laser ranging applications the receiver includes a large diameter telescope (0.5 m or more) and, thus, downlink scintillation was assumed negligible owing to aperture averaging.

Measurements of scintillation in a vertical path from a ground-based laser transmitter to the GEOS-III satellite (orbiting at 1800 to 2000 km) and back to ground were reported by Bufton [19] and compared with the theoretical model developed by Bufton et al. [18]. The laser in this experiment was a CW argon-ion laser operating at $0.514\text{ }\mu\text{m}$. However, a full beam divergence of 0.6 mrad was necessary to provide an adequate pointing error margin. The experimental data for the normalized variance were generally within a factor of 2–4 of the theoretical predictions.

In 1983, Yura and McKinley [20] published a theoretical study of fades and surges for a ground-to-space link in which the transmitted wave was a spherical wave operating in the $1\text{--}10\text{ }\mu\text{m}$ wavelength regime. This analysis, based on weak fluctuation conditions, included estimates of the fraction of time that the signal power is below or above a given threshold value, the mean number of times per second the signal power crosses a given signal level, and the mean duration of fades or surges for a specified variance of log intensity. They also calculated the temporal power spectrum of irradiance based on a frozen-in model of turbulence.

In the Strategic Defense Initiative Organization (SDIO) Relay Mirror Experiment (RME) in the early 1990s, three laser beams (two argon-ion laser beams at $0.488\text{ }\mu\text{m}$ and $0.514\text{ }\mu\text{m}$ and a Nd:YAG laser beam at $1.06\text{ }\mu\text{m}$ wavelength) were projected from two ground sites at AMOS in Hawaii [3]. These beams were both retroreflected and reflected from the RME satellite at 350 km. The uplink beam intensity profile at the satellite appeared as a moderately distorted form of an idealized Gaussian-beam profile. The apparent distortions were attributed to pointing drifts. Measurements of the intensity fluctuations or scintillations as a function of radial distance from the optical axis were in agreement with theoretical predictions.

Shelton [5] published expressions in 1995 for the variance and the power spectral density of turbulence-induced log-amplitude fluctuations associated with an uplink Gaussian-beam wave. The Rytov approximation combined with Mellin transform techniques formed the basis of this theoretical analysis. Experimental data obtained from the Short Wavelength Adaptive Techniques (SWAT) system in Hawaii using an argon-ion cw laser operating at $0.488\text{ }\mu\text{m}$ wavelength were shown to compare well with theoretical predictions. The target used for this data was the Low Power Atmospheric Compensation Experiment (LACE) satellite developed by the Naval Research Laboratory.

Also in 1995, Andrews et al. [4] derived estimates for the beam spot size, scintillation index, fractional fade time, expected number of fades, and mean duration of fade time associated with both uplink and downlink propagation channels for a laser satellite communication system in GEO. This analysis, based on a Gaussian-beam model for the optical wave and a Kolmogorov spectrum for refractive-index fluctuations, used the Rytov approximation and the $H\text{-}V_{5/7} C_n^2$ profile model described by Eq. (1) with $v = 21$ m/s and $A = 1.7 \times 10^{-14} \text{ m}^{-2/3}$. Of particular significance, this study revealed that even small pointing errors with finite beams can lead to unacceptable fade levels owing to a Gaussian roll-off in the mean irradiance profile combined with large off-axis scintillations.

In 1996, Tyson [21] studied the use of adaptive optics in ground-to-space communications and found that signal fades could be significantly reduced. In particular, he concluded that a GEO uplink signal fade can be reduced by a factor of 3 using a ground-based adaptive optics system with more than 50 actuators.

As found in several of the above studies, the implied uplink scintillation index deduced from Rytov theory leads to greatly reduced values of scintillation (orders of magnitude reduction) on the boresight or optical axis of a ground to space collimated beam in which the transmitter beam diameter is on the order of 20–100 cm [4,5,15]. However, none of these earlier studies took into account the possible effects on scintillation that arise from beam jitter associated with beam wander (see Section 8.3). Because the beam width will generally stay smaller than the outer scale of turbulence, the beam may exit the “effective” top of the atmospheric layer (~ 20 km) with a considerable change in direction, leading to significant beam wander (e.g., more than $5 \mu\text{rad}$).

In a more recent uplink numerical wave optics simulation study, Dios et al. [22] showed that the on-axis log-amplitude variance of a collimated beam from ground to space can be much greater than that predicted by conventional Rytov theory when beam wander is present. Dios et al. argue that beam-wander-induced scintillation must be added to the Rytov approximation in such cases. Baker and Benson [23] also showed similar discrepancies in the on-axis scintillation between that predicted by conventional Rytov theory and their numerical wave-optics simulation results in an uplink path to an altitude of 300 km. Again, the conclusion reached by Baker and Benson is that a large reduction in the on-axis scintillation index of an intermediate-size collimated beam as predicted by conventional Rytov theory cannot be achieved in the presence of significant beam wander. By adding wander tracking to the wave optics simulation, the on-axis simulation results and Rytov theory were in better agreement. Off-axis irradiance fluctuations predicted by Rytov theory away from the beam center and the numerical simulation results in [23] were in closer agreement in the presence of beam wander, but the simulation results were generally below that of the Rytov theory. However, wander tracking of the beam led to greatly reduced off-axis scintillation from the numerical code as compared with Rytov theory results.

12.3.3 Pointing and tracking

Prior to data transmission in a space communication system, it is important that the transmitter be properly aimed at the receiver and the receiver detector be aligned with the angle of arrival of the incoming wave. The operation of aiming the transmitter in the proper direction is called *pointing*, and the operation of aiming the receiver lens in the arrival direction of the beam wave is called *spatial acquisition*. Maintaining pointing and acquisition throughout the communication time period is referred to as *spatial tracking*. For narrow optical beams over long distances, the problems of pointing and tracking are particularly critical as compared with longer wavelength RF signals.

One of the major sources of pointing errors is what is called *boresight error*. Basically, this arises from stress, noise, structure fabrication, and so on, in the electronic or mechanical telescope apparatus. Other sources of pointing error are uncertainty in the line-of-sight direction due to reference frame errors and the inability to compensate exactly for transmitter or receiver motion. However, of particular importance is the pointing error caused by atmospheric turbulence. Additional beam spreading due to atmospheric effects causes a dilution of the available power for an uplink channel, and beam wander can result in the beam missing the target altogether. Uplink beam wander angles are typically on the order of a few microradians, but can be much larger for slant paths with zenith angles exceeding 45° . Pointing errors, whether caused by atmospheric effects or other mechanisms, are particularly deleterious to an optical communication channel because of the increase in fade probability of the signal level [4].

In some cases motion of the satellite relative to the ground must be taken into account. For example, a ground-based transmitter must allow for the motion of the satellite that occurs during the transit time of the tracking beam from the satellite to the ground plus that of the transmitted beam back to the satellite. The ground-based transmitter is then pointed at the position where the satellite will be when the beam arrives (see Fig. 12.4). This pointing procedure, called *point ahead*, requires a point-ahead angle $\theta_p \cong 2V/c$, where V is the speed of the satellite perpendicular to the line of sight and c is the speed of light. In the case of a LEO satellite moving at a speed of ~ 7 km/s, this leads to a point-ahead angle of ~ 50 μ rad.

12.3.4 Optical wave models

Following the notation introduced in Chap. 4, we once again introduce the basic Gaussian-beam wave model used in our analysis. The transmitted optical wave model is assumed to be a lowest-order mode paraxial Gaussian-beam wave with unit amplitude. In the absence of optical turbulence, such a Gaussian beam received at distance L from the transmitter can be described by the *input-plane beam parameters*

$$\Theta_0 = 1 - \frac{L}{F_0}, \quad \Lambda_0 = \frac{2L}{kW_0^2}, \quad (8)$$

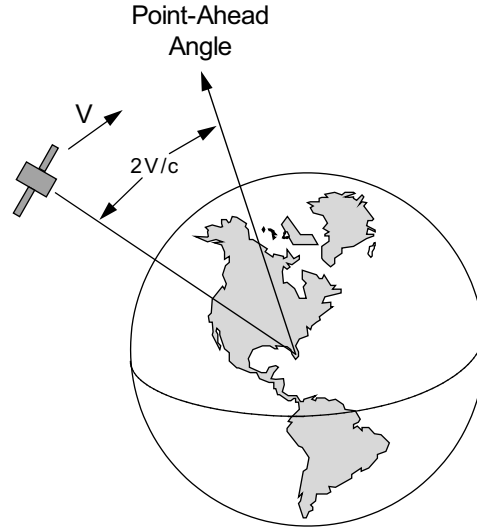


Figure 12.4 Geometry for a point-ahead propagating laser beam.

where W_0 and F_0 denote, respectively, the beam radius and phase front radius of curvature at the transmitter output aperture, $k = 2\pi/\lambda$ is the optical wave number, and λ is the wavelength. The beam incident on the receiver plane is described by the related output-plane *beam parameters*

$$\begin{aligned}\Theta &= 1 + \frac{L}{F} = \frac{\Theta_0}{\Theta_0^2 + \Lambda_0^2}, \\ \bar{\Theta} &= 1 - \Theta, \\ \Lambda &= \frac{2L}{kW^2} = \frac{\Lambda_0}{\Theta_0^2 + \Lambda_0^2},\end{aligned}\tag{9}$$

where $W = W_0\sqrt{\Theta_0^2 + \Lambda_0^2} = W_0/\sqrt{\Theta^2 + \Lambda^2}$ is the diffractive beam radius at the receiver and F is the corresponding phase front radius of curvature. Thus, the free-space irradiance profile of the Gaussian beam at the receiver is

$$I^0(r, L) = \frac{W_0^2}{W^2} \exp\left(-\frac{2r^2}{W^2}\right).\tag{10}$$

In the presence of atmospheric turbulence under weak fluctuation conditions (i.e., the scintillation index is less than unity), we can consider

linear combinations of the following moments of the complex phase perturbations [24]:

$$E_1(0,0) = -2\pi^2 k^2 \sec(\zeta) \int_{h_0}^H \int_0^\infty \kappa \Phi_n(\kappa, h) d\kappa dh, \quad (11)$$

$$E_2(\mathbf{r}_1, \mathbf{r}_2) = 4\pi^2 k^2 \sec(\zeta) \int_{h_0}^H \int_0^\infty \kappa \Phi_n(\kappa, h) \exp\left(-\frac{\Lambda L \kappa^2 \xi^2}{k}\right) \\ \times J_0[\kappa|(1 - \overline{\Theta}\xi)\mathbf{p} - 2i\Lambda\xi\mathbf{r}|] d\kappa dh, \quad (12)$$

$$E_3(\mathbf{r}_1, \mathbf{r}_2) = -4\pi^2 k^2 \sec(\zeta) \int_{h_0}^H \int_0^\infty \kappa \Phi_n(\kappa, h) \exp\left(-\frac{\Lambda L \kappa^2 \xi^2}{k}\right) \\ \times J_0[(1 - \overline{\Theta}\xi - i\Lambda\xi)\kappa\rho] \exp\left[-\frac{iL\kappa^2}{k}\xi(1 - \overline{\Theta}\xi)\right] d\kappa dh, \quad (13)$$

where $J_0(x)$ is a Bessel function (see Appendix I), $\Phi_n(\kappa, h)$ is the spectrum of refractive-index fluctuations, \mathbf{r}_1 and \mathbf{r}_2 are vectors in the transverse direction at the receiver plane, $\mathbf{p} = \mathbf{r}_1 - \mathbf{r}_2$, $\mathbf{r} = \frac{1}{2}(\mathbf{r}_1 + \mathbf{r}_2)$, $\rho = |\mathbf{p}|$, and $*$ denotes the complex conjugate of the quantity. We define the normalized distance variable ξ for uplink and downlink propagation according to

$$\xi = 1 - \left(\frac{h - h_0}{H - h_0}\right), \quad (\text{uplink propagation}) \\ \xi = \left(\frac{h - h_0}{H - h_0}\right), \quad (\text{downlink propagation}) \quad (14)$$

where h_0 is the height above ground level of the uplink transmitter and/or downlink receiver, $H = h_0 + L \cos(\zeta)$ is the satellite altitude, and ζ is the zenith angle. Although the general development does not depend on the choice of spectrum model, most numerical results presented in this chapter are based on the *Kolmogorov power-law spectrum*

$$\Phi_n(\kappa, h) = 0.033 C_n^2(h) \kappa^{-11/3}, \quad (15)$$

where $C_n^2(h)$ is a function of altitude h .

12.4 Second-Order Statistics

To begin our investigation of various second-order statistical quantities, such as the spatial coherence radius, angle-of-arrival fluctuations, and isoplanatic angle, we once again consider specializations of the *mutual coherence function* (MCF). In this section we treat both uplink and downlink paths.

12.4.1 Spatial coherence radius

The MCF is closely related to the *wave structure function* (WSF), which is dominated by the phase structure function. For observation points symmetrically located within the beam spot size ($\mathbf{r}_2 = -\mathbf{r}_1$), the WSF for a Gaussian-beam wave on either an uplink or downlink path is defined by (see Section 6.4.3)

$$\begin{aligned} D(\rho, L) &= 2[E_2(\mathbf{r}, \mathbf{r}) - E_2(\mathbf{r}, -\mathbf{r})] \\ &= 8\pi^2 k^2 \sec(\zeta) \int_{h_0}^H \int_0^\infty \kappa \Phi_n(\kappa, h) \exp\left(-\frac{\Lambda L \kappa^2 \xi^2}{k}\right) \\ &\quad \times \{I_0(\Lambda \rho \xi \kappa) - J_0[(1 - \bar{\Theta} \xi) \kappa \rho]\} d\kappa dh, \end{aligned} \quad (16)$$

where ρ is separation distance between observation points and $I_0(x) = J_0(ix)$ is a modified Bessel function (see Appendix I). Upon evaluation, Eq. (16) for a *downlink* channel leads to the approximate expression

$$D(\rho, L) = 2.91 k^2 \rho^{5/3} \sec(\zeta) (\mu_{1d} + 0.62 \mu_{2d} \Lambda^{11/6}), \quad (17)$$

where we have incorporated the approximation $(k\rho^2/L)^2 \cong (k\rho^2/L)^{5/3}$ and where

$$\mu_{1d} = \int_{h_0}^H C_n^2(h) \left[\Theta + \bar{\Theta} \left(1 - \frac{h - h_0}{H - h_0} \right) \right]^{5/3} dh, \quad (18)$$

$$\mu_{2d} = \int_{h_0}^H C_n^2(h) \left(\frac{h - h_0}{H - h_0} \right)^{5/3} dh. \quad (19)$$

Both expressions (18) and (19) emphasize high-altitude turbulence which is weak. Thus, for an optical wave from space ($H \gg 20$ km), we find that $\mu_{1d} \cong \mu_0$ and $\mu_{2d} \cong 0$, reducing (17) essentially to that of a plane wave, viz.,

$$D(\rho, L) = 2.91 k^2 \rho^{5/3} \mu_0 \sec(\zeta), \quad (20)$$

where

$$\mu_0 = \int_{h_0}^H C_n^2(h) dh. \quad (21)$$

Other statistical quantities associated with a beam wave (or starlight) from space also behave much like an infinite plane wave at the point where light enters the atmospheric layer (at ~ 20 km altitude). Consequently, the plane wave model is often assumed in various theoretical analyses involving downlink channels.

We define the spatial coherence radius as that separation distance ρ in which $D(\rho, L) = 2$. Hence, the implied *spatial coherence radius* deduced from (20) is

$$\rho_0 = \left(\frac{\cos \zeta}{1.45 \mu_0 k^2} \right)^{3/5}. \quad (22)$$

The spatial coherence radius (22) for a downlink path is generally on the order of a few centimeters for wavelengths $\lambda \sim 1 \mu\text{m}$ and zenith angles not exceeding 60 deg. In many applications it is customary to introduce the *atmospheric coherence width* $r_0 = 2.1\rho_0$ in place of the spatial coherence radius. The parameter r_0 , also called *Fried's parameter* (see Chap. 14), is usually defined by the expression

$$r_0 = \left[0.42 \sec(\zeta) k^2 \int_{h_0}^H C_n^2(h) dh \right]^{-3/5}. \quad (23)$$

In the case of an *uplink* channel, Eq. (16) yields the approximate result

$$D(\rho, L) = 2.91 k^2 \rho^{5/3} \sec(\zeta) (\mu_{1u} + 0.62 \mu_{2u} \Lambda^{11/6}), \quad (24)$$

where

$$\mu_{1u} = \int_{h_0}^H C_n^2(h) \left[\Theta + \overline{\Theta} \left(\frac{h - h_0}{H - h_0} \right) \right]^{5/3} dh, \quad (25)$$

$$\mu_{2u} = \int_{h_0}^H C_n^2(h) \left(1 - \frac{h - h_0}{H - h_0} \right)^{5/3} dh. \quad (26)$$

Based on Eq. (24) for the WSF, the implied spatial coherence radius ρ_0 for the optical wave on an uplink path is given by

$$\rho_0 = \left[\frac{\cos \zeta}{1.46 k^2 (\mu_{1u} + 0.622 \mu_{2u} \Lambda^{11/6})} \right]^{3/5}. \quad (27)$$

For an uplink path, the spatial coherence radius at the satellite will be many times larger than the probable size of the satellite.

Whereas the above results are based on a Kolmogorov spectrum, the effect of non-Kolmogorov turbulence in the stratosphere on the spatial coherence radius and star image motion has been theoretically investigated by Gurvich and Belen'kii [25]. The conclusion drawn from this study was that stratospheric turbulence does not degrade short-exposure images, but does degrade long-exposure ones. Experimental verification of the effect of non-Kolmogorov turbulence on star image motion was observed by Belen'kii et al. [26].

12.4.2 Angle-of-arrival fluctuations

Angle-of-arrival fluctuations for uplink and downlink paths can be deduced directly from knowledge of the WSF (Section 6.5). Based on the above expressions and a receiver aperture of diameter $2W_G$, the variance of the angle-of-arrival fluctuations becomes

$$\langle \beta_a^2 \rangle \cong \begin{cases} 2.91 \mu_0 \sec(\zeta) (2W_G)^{-1/3} & \text{(downlink)} \\ 2.91 (\mu_{1u} + 0.62 \mu_{2u} \Lambda^{11/6}) \sec(\zeta) (2W_G)^{-1/3} & \text{(uplink).} \end{cases} \quad (28)$$

Because the dominant parameter appearing in the lower expression in (28) is defined primarily by high-altitude weak turbulence conditions, the root-mean-square (rms) angle of arrival deduced from (28) for an uplink path is generally $< 1 \mu\text{rad}$. For a downlink path, the rms angle of arrival deduced from the upper expression in (28) is independent of wavelength and, unlike an uplink channel, is generally on the order of several microradians.

12.4.3 Isoplanatic angle

The principle behind adaptive optics imaging systems is to sense the phase distortions of a known source and apply a (“corrective” or conjugate phase to the outgoing beam or incoming image. The angular distance (from a reference beacon) over which atmospheric turbulence is essentially unchanged is called the *isoplanatic angle* θ_0 . If a propagating beam is offset by a constant angle from the direction along which the atmospheric turbulence is measured, the effect is called *angular anisoplanatism* [27–30]. For an upward-propagating Gaussian-beam wave, the isoplanatic angle is defined by

$$\theta_0 = \frac{\cos^{8/5}(\zeta)}{(H - h_0)[2.91k^2(\mu_{1u} + 0.62 \mu_{2u}\Lambda^{11/6})]^{3/5}}, \quad (29)$$

and in the special case of a spherical wave ($\Theta = \Lambda = 0$), Eq. (29) reduces to

$$\theta_0 = \frac{\cos^{8/5}(\zeta)}{\left[2.91k^2 \int_{h_0}^H C_n^2(h)(h - h_0)^{5/3} dh\right]^{3/5}}. \quad (30)$$

Another example of angular anisoplanatism occurs when a moving uncooperative satellite target is being tracked by one beam and another is used to intercept the target in a point-ahead configuration. In this setting the point-ahead angle, which must allow for transit time from the satellite to the ground and back again, is $\theta_p \cong 2V/c$ (Fig. 12.4). Thus, the point-ahead angle is typically on the order of $50 \mu\text{rad}$, which is ordinarily much larger than the isoplanatic angle from the tracking direction (see Fig. 12.5). In practice, therefore, a measurement of the wave-front along the tracking path is useless in correcting for the turbulence along the propagation path. Instead, a synthetic beacon or laser guide star closer to the propagation path can provide more useful information about wave-front distortions.¹

12.5 Irradiance Statistics: Downlink Channel

In this section we investigate the mean irradiance of a downlink wave in the plane of the receiver from which we infer the effective beam spot size.

¹In one experimental study [26], it was suggested that the concept of isoplanatic angle is not applicable to tilt-related phenomenon. In this case, the isoplanatic angle cannot be used for the analysis of the effect of the point-ahead angle on the performance of tracking systems.

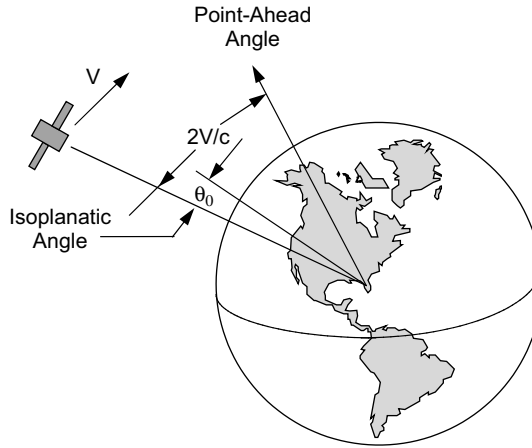


Figure 12.5 Geometry for a point-ahead propagating beam and the isoplanatic angle.

In addition, expressions are developed for the corresponding scintillation index and covariance function of irradiance. Most numerical calculations are based on the H- $V_{5/7}$ atmospheric model [Eq.(1) with $A = 1.7 \times 10^{-14} \text{ m}^{-2/3}$ and $w = 21 \text{ m/s}$].

12.5.1 Mean irradiance

The *mean irradiance* of the optical wave at the pupil plane of the receiver for either an uplink or downlink channel can be expressed as

$$\begin{aligned} \langle I(\mathbf{r}, L) \rangle &= I^0(\mathbf{r}, L) \langle \exp[\psi(\mathbf{r}, L) + \psi^*(\mathbf{r}, L)] \rangle \\ &= I^0(\mathbf{r}, L) \exp[2E_1(0, 0) + E_2(\mathbf{r}, \mathbf{r})], \end{aligned} \quad (31)$$

where $I^0(\mathbf{r}, L)$ is defined by Eq. (10) and the quantities $E_1(0, 0)$ and $E_2(\mathbf{r}, \mathbf{r})$ are defined, respectively, by Eqs. (12) and (13). Previous work has shown that the mean irradiance can be closely approximated by a Gaussian spatial profile [3,31] (see also Chap. 6). Thus, we can write Eq. (31) in the form

$$\langle I(\mathbf{r}, L) \rangle = \frac{W_0^2}{W_{LT}^2} \exp\left(-\frac{2r^2}{W_{LT}^2}\right), \quad (32)$$

where W_{LT} is the effective or long-term spot size of the Gaussian beam in the presence of optical turbulence.

For a *downlink* path the *long-term spot size* is

$$\begin{aligned} W_{LT} &= W\sqrt{1 + T} \\ &= W\left[1 + 4.35\mu_{2d}\Lambda^{5/6}k^{7/6}(H - h_0)^{5/6}\sec^{11/6}(\zeta)\right]^{1/2}, \end{aligned} \quad (33)$$

where

$$T = -2E_1(0,0) - E_2(0,0) \\ = 4\pi^2 k \sec(\zeta) \int_{h_0}^H \int_0^\infty \kappa \Phi_n(h, \kappa) \left[1 - \exp\left(-\frac{\Lambda L \kappa^2 \xi^2}{k}\right) \right] d\kappa dh. \quad (34)$$

Because the parameter μ_{2d} emphasizes only weak high-altitude turbulence, we can once again set $\mu_{2d} \cong 0$ for almost any downlink path. We deduce, therefore, that the long-term spot size for a downlink beam may be essentially the same as its diffractive spot size, i.e., $W_{LT} \cong W$. For some long, low elevation paths, however, it may turn out that μ_{2d} cannot be set to zero in which case it will be necessary to use (33).

12.5.2 Scintillation index

The *scintillation index* plays an important role in satellite communication systems. From weak fluctuation theory, the scintillation index can be expressed as (Section 8.2)

$$\sigma_I^2(\mathbf{r}, L) \cong 2\text{Re}[E_2(\mathbf{r}, \mathbf{r}) + E_3(\mathbf{r}, \mathbf{r})], \quad (35)$$

where $E_2(\mathbf{r}_1, \mathbf{r}_2)$ and $E_3(\mathbf{r}_1, \mathbf{r}_2)$ are defined by Eqs. (12) and (13) and Re denotes the real part of the argument. Based on (12), (13), and (35), the scintillation index for a *downlink* channel is therefore given by

$$\sigma_I^2(\mathbf{r}, L) = 14.53\mu_{2d}\Lambda^{5/6}k^{7/6}(H-h_0)^{17/6}\sec^{23/6}(\zeta)\frac{\alpha_r^2}{W^2} \\ + 8.70\mu_{3d}k^{7/6}(H-h_0)^{5/6}\sec^{11/6}(\zeta), \quad \alpha_r \leq W/L, \quad (36)$$

where $\alpha_r = r/L$,

$$\mu_{3d} = \text{Re} \int_{h_0}^H C_n^2(h) \left\{ \xi^{5/6} [\Lambda \xi + i(1 - \overline{\Theta} \xi)]^{5/6} - \Lambda^{5/6} \xi^{5/3} \right\} dh, \quad (37)$$

and where $\xi = (h - h_0)/(H - h_0)$. For the case in which $H \gg 20$ km, the scintillation index is essentially that of an *unbounded plane wave* ($\Theta = 1$, $\Lambda = 0$). Thus, for a downlink path from space, we can generally replace Eqs. (36) and (37) with the simpler plane wave expression

$$\sigma_I^2(r, L) = \sigma_R^2 = 2.25k^{7/6}\sec^{11/6}(\zeta) \int_{h_0}^H C_n^2(h)(h-h_0)^{5/6} dh. \quad (38)$$

If we use the H-V_{5/7} turbulence model, wavelength $\lambda = 1.55 \mu\text{m}$, and zenith angles $0^\circ \leq \zeta \leq 60^\circ$, the scintillation index derived from (36) [or (38)] across the beam profile on a downlink channel is typically $\sigma_I^2(\mathbf{r}, L) \sim 0.07$ to 0.23 out to the diffraction-limited beam edge, regardless of initial beam size. Because off-axis fluctuations are nearly the same as on-axis for most of the diffraction-limited spot size, the effect of a pointing error on signal fading for a

downlink path (see Section 12.7) will depend largely on changes in the mean irradiance owing to a Gaussian profile. As a consequence, it can be shown that beam wander is not an issue for a downlink path from space.

Aperture averaging of scintillation can occur whenever the aperture of the receiver is sufficiently large, i.e., larger than the transverse irradiance correlation width ρ_c (see Section 12.5.3). In this case with $H \gg 20$ km, we find that the irradiance flux variance in the plane of the receiver photodetector can be calculated by use of the *ABCD* matrix approach illustrated in Chap. 10. In particular, the *irradiance flux variance* in the focal plane of a receiver can be approximated by the plane wave expression

$$\sigma_I^2(D_G) = 8.70k^{7/6}(H - h_0)^{5/6} \sec^{11/6}(\zeta) \times \operatorname{Re} \int_{h_0}^H C_n^2(h) \left[\left(\frac{kD_G^2}{16L} + i \frac{h - h_0}{H - h_0} \right)^{5/6} - \left(\frac{kD_G^2}{16L} \right)^{5/6} \right] dh, \quad (39)$$

where D_G is the “hard aperture” diameter of the receiver lens. In Fig. 12.6 we illustrate the irradiance flux variance for a collimated Gaussian-beam wave transmitted from space as a function of aperture diameter D_G for zenith angles of 45 deg (solid curve) and 60 deg (dashed curve). We have assumed the receiver is on the ground ($h_0 = 0$) and have used the H-V_{5/7} model for $C_n^2(h)$. When $D_G = 0$ (point receiver case), Eq. (39) reduces to the scintillation index of an infinite plane wave (38).

For larger zenith angles the downlink scintillation index can exceed the limitations of weak fluctuation theory. In the general case including

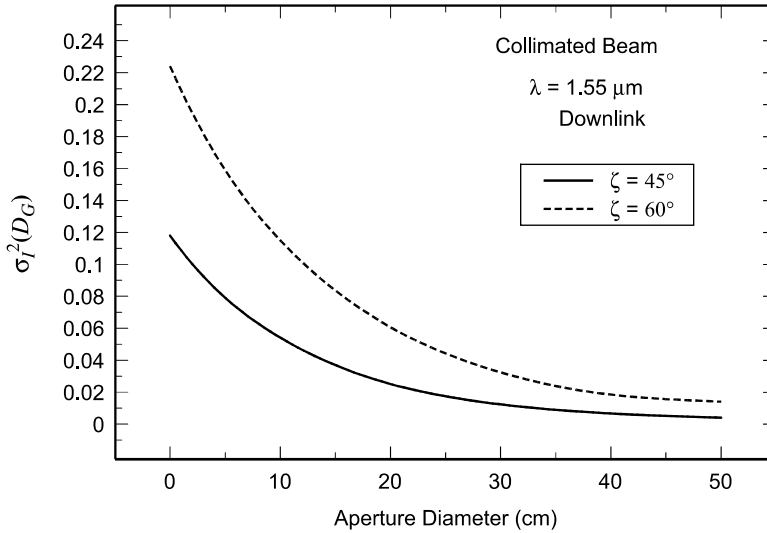


Figure 12.6 Downlink irradiance flux variance of a collimated beam wave from space as a function of aperture diameter D_G .

moderate-to-strong irradiance fluctuations, the scintillation index throughout the center portion of the beam on a downlink channel with a point receiver is given by [32,33]

$$\sigma_I^2(0, L) = \exp \left[\frac{0.49 \sigma_R^2}{\left(1 + 1.11 \sigma_R^{12/5}\right)^{7/6}} + \frac{0.51 \sigma_R^2}{\left(1 + 0.69 \sigma_R^{12/5}\right)^{5/6}} \right] - 1, \quad (40)$$

$$0 \leq \sigma_R^2 < \infty,$$

where σ_R^2 is defined by (38). Note that this last expression has the same functional form as that for a plane wave propagating along a horizontal path in which the structure parameter C_n^2 is constant (see Section 9.4.1).

For a satellite positioned in space with a receiver on the ground ($h_0 = 0$), the scintillation index (40) varies with zenith angle as shown in Fig. 12.7 for a downlink optical wave with wavelength $\lambda = 1.06 \mu\text{m}$. Weak fluctuation theory (dotted curves) as predicted by (38) is valid only for zenith angles less than 60 deg when ground level turbulence is of the order of $A = 1.7 \times 10^{-14} \text{m}^{-2/3}$. However, when ground-level turbulence satisfies $A = 3 \times 10^{-13} \text{m}^{-2/3}$, weak fluctuation theory is restricted to zenith angles < 40 deg. For shorter wavelengths, weak fluctuation theory is limited to even smaller zenith angles.

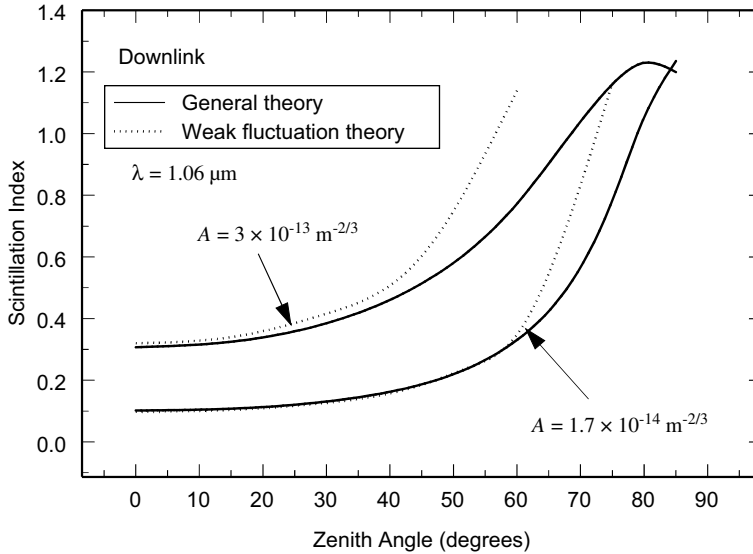


Figure 12.7 Downlink scintillation index of a plane wave from space (solid lines) as a function of zenith angle and two values of ground level $A = C_n^2(0)$. The dotted curves depict weak fluctuation theory results.

12.5.3 Covariance function of irradiance

The *transverse correlation width* ρ_c associated with the irradiance of a Gaussian-beam wave in the plane of the receiver is usually estimated by one of the following—the $1/e$ point, $1/e^2$ point, or zero crossing point of the normalized *covariance function*. For example, the zero crossing point is used for weak irradiance fluctuations, but the $1/e$ or $1/e^2$ point is generally used under strong fluctuations. Under weak irradiance fluctuations, the normalized covariance function for a downlink channel can be expressed as

$$b_I(\rho, L) = \frac{B_I(\rho, L)}{B_I(0, L)} = \frac{\mu_{3d}(\rho)}{\mu_{3d}(0)}, \quad (41)$$

where $\rho = |\mathbf{r} - (-\mathbf{r})| = 2r$ is the distance between two points symmetrically located with respect to the optical axis, $\mu_{3d}(0) = \mu_{3d}$ is defined by Eq. (37), and

$$\begin{aligned} \mu_{3d}(\rho) = \text{Re} \int_{h_0}^H C_n^2(h) \left[\xi^{5/6} [\Lambda \xi + i(1 - \bar{\Theta} \xi)]^{5/6} {}_1F_1 \left\{ -\frac{5}{6}; 1; -\frac{kp^2(1 - \bar{\Theta} \xi - i\Lambda \xi)^2}{4L\xi[\Lambda \xi + i(1 - \bar{\Theta} \xi)]} \right\} \right. \\ \left. - (\Lambda \xi^2)^{5/6} {}_1F_1 \left[-\frac{5}{6}; 1; -\frac{kp^2}{4L\Lambda} \left(\frac{1 - \bar{\Theta} \xi}{\xi} \right)^2 \right] \right] dh. \end{aligned} \quad (42)$$

In Eq. (42), the function ${}_1F_1(a; c; x)$ is the confluent hypergeometric function (see Appendix I) and $\xi = (h - h_0)/(H - h_0)$.

The implied transverse correlation width ρ_c at the receiver for a downlink propagation path is typically on the order of only 7–10 cm, depending on wavelength. These findings are consistent with measurements reported by Lightsey [3]. Moreover, it has been found that the correlation width under weak irradiance fluctuations can be reasonably approximated by the empirical formula [32]

$$\rho_c \cong \sqrt{\frac{45 \times 10^3 \sec(\zeta)}{k}}, \quad \sigma_R^2 \ll 1, \quad 0 \leq \zeta < 50^\circ. \quad (43)$$

For a downlink path from a satellite, including the case of a large zenith angle, it has been shown that the covariance function can be approximated by [32]

$$\begin{aligned} B_I(\rho) &= \exp[B_{\ln X}(\rho) + B_{\ln Y}(\rho)] - 1 \\ &= \exp \left[\frac{\mu_{4d}(\rho)}{\mu_{4d}(0)} \sigma_{\ln X}^2 + 0.99 \left(\frac{kp^2 \eta_Y}{L} \right)^{5/12} K_{5/6} \left(\sqrt{\frac{kp^2 \eta_Y}{L}} \right) \sigma_{\ln Y}^2 \right] - 1, \end{aligned} \quad (44)$$

where

$$\mu_{4d}(\rho) = \int_{h_0}^H \frac{C_n^2(h)}{\xi^{1/3} (1 - \frac{5}{8} \xi)^{7/5}} {}_1F_1 \left[\frac{7}{5}; 1; \frac{-kp^2 \eta_X}{8L\xi^{5/3} (1 - \frac{5}{8} \xi)} \right] dh. \quad (45)$$

The first term in the argument of the exponential function in (44) corresponds to the large-scale fluctuations, the second term to the small-scale fluctuations, and

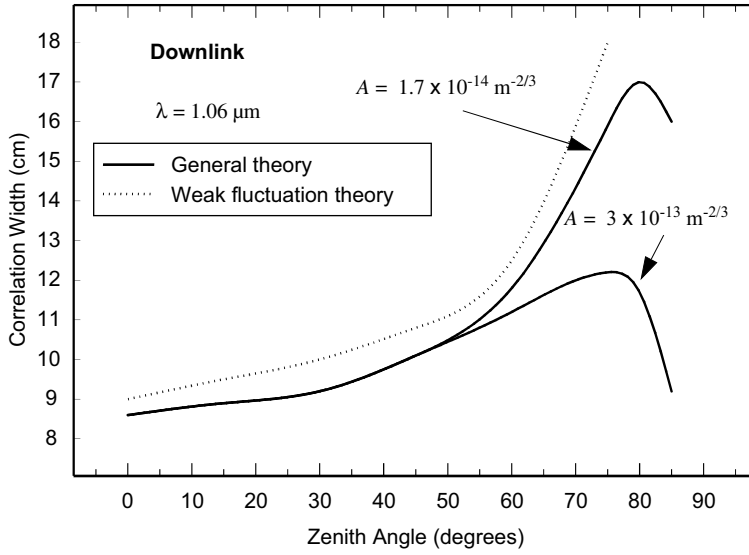


Figure 12.8 Correlation width ρ_c shown as a function of zenith angle for a downlink propagation path from a satellite in orbit.

$K_v(x)$ is a modified Bessel function of the second kind. Also, we have introduced the notation

$$\eta_X = \frac{0.92}{1 + 1.11\sigma_R^{12/5}}, \quad \eta_Y = 3(1 + 0.69\sigma_R^{12/5}), \quad (46)$$

$$\sigma_{\ln X}^2 = \frac{0.49\sigma_R^2}{(1 + 1.11\sigma_R^{12/5})^{7/6}}, \quad \sigma_{\ln Y}^2 = \frac{0.51\sigma_R^2}{(1 + 0.69\sigma_R^{12/5})^{5/6}}, \quad (47)$$

where σ_R^2 is defined by (38).

In Fig. 12.8 we show the implied correlation width (solid curves) of a ground-based receiver associated with a downlink communication path from a LEO satellite. Notice the two curves, corresponding to $A = 1.7 \times 10^{-14} \text{ m}^{-2/3}$ and $A = 3 \times 10^{-13} \text{ m}^{-2/3}$, coincide under weak fluctuation conditions (zenith angles not exceeding 50 deg). Also shown in Fig. 12.8 for comparison is the implied correlation width (dotted curve) derived from standard Rytov weak fluctuation theory, based on the zero crossing point of the normalized covariance function. The small distinction between the weak fluctuation result and that deduced from (44) is that the latter is based on the $1/e$ point rather than a zero crossing.²

²Although the results shown in Fig. 12.8 (solid curves) are based on a LEO satellite using the $1/e$ point of the normalized covariance function, the same results are deduced for a GEO satellite by using the half-power point of the normalized covariance function rather than the $1/e$ point. This particular sensitivity of the model to the altitude of the satellite in predicting the correlation width is simply a peculiarity of the theoretical model itself.

12.6 Irradiance Statistics: Uplink Channel

A schematic of the ground/space propagation channel under consideration is provided in Fig. 12.9. For an uplink path, we will find that beam wander begins to play an important role, not only in producing a large long-term spot size, but also in producing an “effective pointing error” that leads to increased on-axis irradiance fluctuations (scintillation) over that predicted by conventional Rytov theory.

12.6.1 Mean irradiance

Using the principle of *reciprocity* (see Section 8.3), the *long-term spot size* for the *uplink* channel under weak and strong irradiance fluctuations takes the form

$$W_{LT} = \begin{cases} W\sqrt{1 + (D_0/r_0)^{5/3}}, & 0 \leq D_0/r_0 < 1 \\ W[1 + (D_0/r_0)^{5/3}]^{3/5}, & 0 \leq D_0/r_0 < \infty \end{cases} \quad (48)$$

where r_0 is the atmospheric coherence width (23) and $D_0^2 = 8W_0^2$. The principle of reciprocity used here is based on the notion that the far-field Strehl ratio

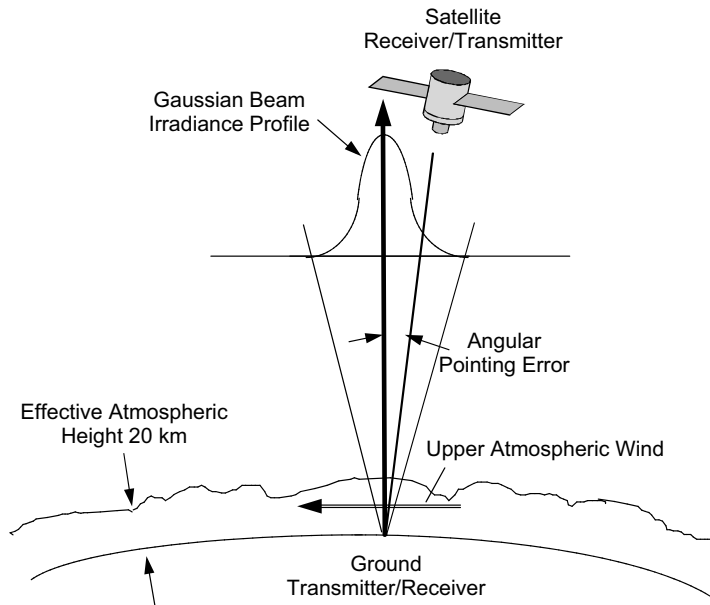


Figure 12.9 Schematic of an uplink propagation channel illustrating the Gaussian-beam profile of the mean irradiance at the satellite and angular pointing error. The effective atmospheric height for the H-V $C_n^2(h)$ profile model is ~ 20 km.

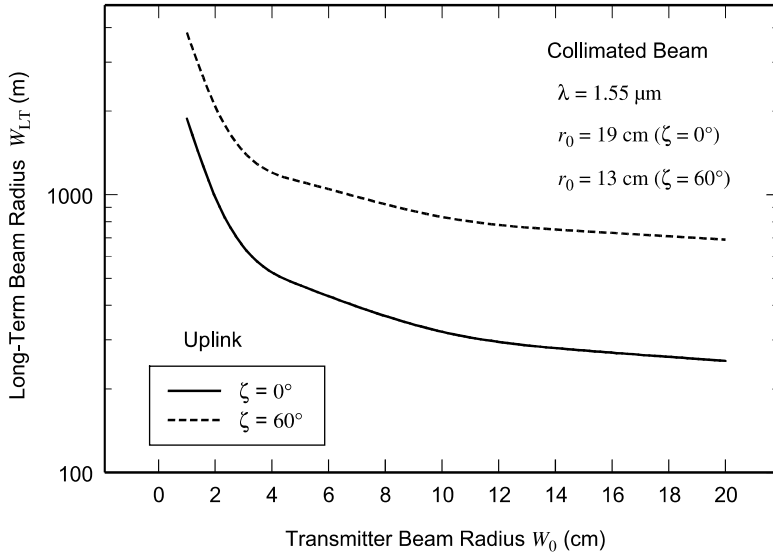


Figure 12.10 Uplink long-term beam radius (in meters) at the receiver of a GEO satellite for two zenith angles ζ and shown as a function of beam radius (in centimeters).

(SR) is defined by the near-field phase variance $\sigma_S^2 \sim (D_0/r_0)^{5/3}$. That is (see Section 10.2.4),

$$SR \cong \begin{cases} [1 + (D_0/r_0)^{5/3}]^{-1}, & 0 \leq D_0/r_0 < 1 \\ [1 + (D_0/r_0)^{5/3}]^{-6/5}, & 0 \leq D_0/r_0 < \infty. \end{cases} \quad (49)$$

Unlike the downlink case, additional beam spreading due to atmospheric turbulence on an uplink path begins close to the transmitter, which in turn causes the beam to be much larger than that associated with pure free-space diffraction effects. For example, the long-term beam radius (48) at a satellite in GEO ($H \sim 38.5 \times 10^3$ km) is shown in Fig. 12.10 as a function of beam radius W_0 at the output aperture of a ground transmitter ($h_0 = 0$) for zenith angles $\zeta = 0^\circ$ and $\zeta = 60^\circ$. This figure reveals that the effective beam size at the satellite decreases rapidly with increasing transmitter beam radius for smaller beams ($1 < W_0 < 4$ cm).

12.6.2 Beam wander

Angular deviations of the beam from the boresight, called *beam wander*, can cause time-varying power fades. Beam wander is of little concern for a downlink path, but on an uplink path it can be large enough to cause the beam to move several hundred meters.

A beam wander displacement model under weak irradiance fluctuations was developed in Chap. 6. Adapted to an uplink path, the *beam wander displacement variance* becomes

$$\begin{aligned} \langle r_c^2 \rangle = & 7.25(H-h_0)^2 \sec^3(\zeta) W_0^{-1/3} \int_{h_0}^H C_n^2(h) \left(1 - \frac{h-h_0}{H-h_0}\right)^2 \\ & \times \left[\frac{1}{\left| \Theta_0 + \bar{\Theta}_0 \left(1 - \frac{h-h_0}{H-h_0}\right) \right|^{1/3}} - \left\{ \frac{\kappa_0^2(h) W_0^2}{1 + \kappa_0^2(h) W_0^2 \left[\Theta_0 + \bar{\Theta}_0 \left(1 - \frac{h-h_0}{H-h_0}\right) \right]^2} \right\} \right]^{1/6} dh, \end{aligned} \quad (50)$$

where $\kappa_0(h) \sim 1/L_0(h)$. For illustrative purposes, we will only consider a *collimated beam* ($\Theta_0 = 1$). In some cases we can also replace the outer scale parameter with a nominal value that leads to the simpler expression

$$\langle r_c^2 \rangle = 0.54(H-h_0)^2 \sec^2(\zeta) \left(\frac{\lambda}{2W_0} \right)^2 \left(\frac{2W_0}{r_0} \right)^{5/3} \left[1 - \left(\frac{\kappa_0^2 W_0^2}{1 + \kappa_0^2 W_0^2} \right)^{1/6} \right], \quad (51)$$

where we have used Eq. (23) in conjunction with the approximation

$$\int_{h_0}^H C_n^2(h) \left(1 - \frac{h-h_0}{H-h_0}\right)^2 dh \cong \int_{h_0}^H C_n^2(h) dh = \mu_0. \quad (52)$$

In Fig. 12.11 we illustrate the effect of the rms angular beam wander $\sqrt{\langle r_c^2 \rangle}/L$ in microradians for various size collimated beams from ground to space. The wavelength is set at $\lambda = 1.55 \mu\text{m}$ (although beam wander is basically independent of wavelength) and the zenith angle is $\zeta = 0$ deg. The solid curve is based on the outer scale model described by Eq. (7) with $\kappa_0(h) = 2\pi/L_0(h)$, and the dashed curve represents the case when the outer scale is infinite ($\kappa_0 = 0$). Here we see that the angular displacement is greatest for smaller beams and steadily decreases with increasing beam radius. Also, we see that the presence of a finite outer scale significantly reduces the amount of beam wander. Last, by selecting a nominal outer-scale value corresponding to $\kappa_0 = 10$ and using Eq. (51), we can generate virtually the same result as that shown by the solid curve in Fig. 12.11.

12.6.3 Scintillation index

Based on first-order Rytov theory, the scintillation index of an *uplink* collimated beam can decrease by orders of magnitude as the transmitted beam radius increases. However, such a reduction in scintillation may actually occur only with perfect removal of beam wander effects. Below we use the models developed in Chap. 8 to examine the ramifications of beam-wander-induced scintillation on a collimated beam along an uplink path.

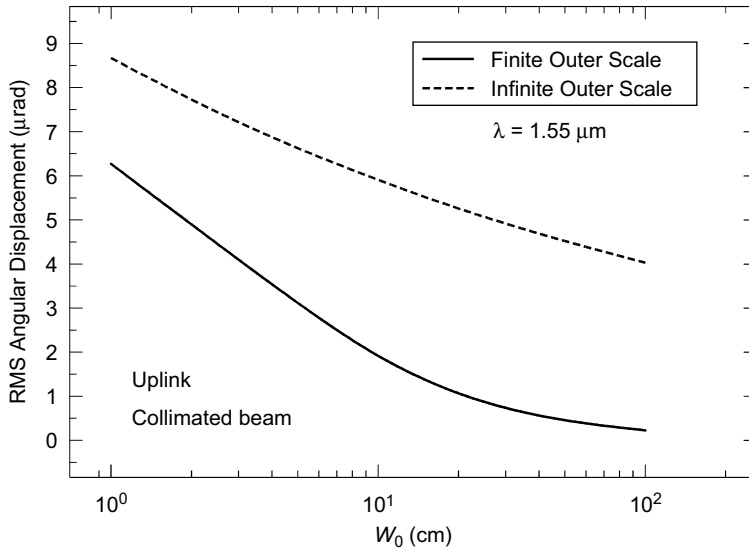


Figure 12.11 The rms angular beam wander in microradians plotted as a function of beam radius at the receiver for a transmitter on the ground and a satellite in space at zenith angle zero.

Adapting the approach in Section 8.3.1 for weak irradiance fluctuations to an uplink propagation path, we start by introducing the *pointing error variance*

$$\begin{aligned}\sigma_{pe}^2 &= 7.25(H - h_0)^2 \sec^3(\zeta) W_0^{-1/3} \\ &\times \left[1 - \left(\frac{\kappa_r^2 W_0^2}{1 + \kappa_r^2 W_0^2} \right)^{1/6} \right] \int_{h_0}^H C_n^2(h) \left(1 - \frac{h - h_0}{H - h_0} \right)^2 dh \\ &\cong 0.54(H - h_0)^2 \sec^2(\zeta) \left(\frac{\lambda}{2W_0} \right)^2 \left(\frac{2W_0}{r_0} \right)^{5/3} \left[1 - \left(\frac{C_r^2 W_0^2 / r_0^2}{1 + C_r^2 W_0^2 / r_0^2} \right)^{1/6} \right], \quad (53)\end{aligned}$$

where C_r is a scaling constant and r_0 is defined by (23). In arriving at the second step in (53) we have approximated the integral by μ_0 and used the reciprocity principle. Thus, the uplink *longitudinal component* of the scintillation index for an *untracked beam* can be expressed in the form

$$\begin{aligned}\sigma_{L,l}^2(L)_{\text{untracked}} &= 5.95(H - h_0)^2 \sec^2(\zeta) \left(\frac{2W_0}{r_0} \right)^{5/3} \left(\frac{\alpha_{pe}}{W} \right)^2 \\ &+ 8.70\mu_{3u}k^{7/6}(H - h_0)^{5/6} \sec^{11/6}(\zeta),\end{aligned} \quad (54)$$

where $\alpha_{pe} = \sigma_{pe}/L$ describes the jitter-induced angular pointing error,

$$\mu_{3u} = \text{Re} \int_{h_0}^H C_n^2(h) \left\{ \xi^{5/6} [\Lambda \xi + i(1 - \overline{\Theta} \xi)]^{5/6} - \Lambda^{5/6} \xi^{5/3} \right\} dh, \quad (55)$$

and $\xi = 1 - (h - h_0)/(H - h_0)$. As discussed in Chap. 8, the longitudinal component (54) is essentially constant throughout a circular disk of radius σ_{pe} centered on the boresight. Beyond this circular disk, the off-axis scintillation is described by

$$\begin{aligned} \sigma_I^2(\mathbf{r}, L)_{\text{untracked}} &= 5.95(H - h_0)^2 \sec^2(\zeta) \left(\frac{2W_0}{r_0} \right)^{5/3} \left(\frac{\alpha_r - \alpha_{pe}}{W} \right)^2 U(\alpha_r - \alpha_{pe}) \\ &+ \sigma_{I,l}^2(L)_{\text{untracked}}, \quad \alpha_r < W/L, \end{aligned} \quad (56)$$

where $\alpha_r = r/L$ and $U(x)$ is the unit step function. To satisfy the conditions of weak fluctuation theory, the radius of the transmitter aperture may be limited to around 20 cm or less, depending upon wavelength and/or zenith angle.

In general, *tracking* a beam can mean either tracking the “hot spot” in the wandering beam or removing tilt, among other schemes. Along a horizontal path these two methods are essentially the same from a theoretical point of view (see Chap. 8), but not so for an uplink path to space. For the theoretical development below, we will only consider tracking as that based on removing the rms hot spot displacement. However, hot-spot tracking of an uplink beam is quite challenging for large beams because they tend to approach saturation of the scintillation index and consequently break up into multiple beams, thereby producing several “hot spots.” For that reason, tracking by tilt-removal is generally used in practice.

In the present case of a *tracked beam*, the scintillation index throughout the beam profile is described by

$$\begin{aligned} \sigma_I^2(\mathbf{r}, L)_{\text{tracked}} &= 8.70\mu_{3u}k^{7/6}(H - h_0)^{5/6} \sec^{11/6}(\zeta) \\ &+ 5.95(H - h_0)^2 \sec^2(\zeta) \left(\frac{2W_0}{r_0} \right)^{5/3} \\ &\times \left(\frac{\alpha_r - \sqrt{\langle \alpha_c^2 \rangle}}{W} \right)^2 U\left(\alpha_r - \sqrt{\langle \alpha_c^2 \rangle}\right), \quad 0 \leq \alpha_r < W/L, \end{aligned} \quad (57)$$

where $\sqrt{\langle \alpha_c^2 \rangle} = \sqrt{\langle r_c^2 \rangle}/L$. The first term on the right-hand side of (57) represents the longitudinal component derived under conventional Rytov theory [4], viz.,

$$\sigma_{I,l}^2(L)_{\text{tracked}} \equiv \sigma_{Bu}^2 = 8.70\mu_{3u}k^{7/6}(H - h_0)^{5/6} \sec^{11/6}(\zeta). \quad (58)$$

In Fig. 12.12 we plot the longitudinal component (54) for a 10-cm radius untracked beam and (58) for the same beam when tracked as a function of altitude h at zenith angle zero. The wavelength is $\lambda = 1.55 \mu\text{m}$, which produces a spatial coherence value $r_0 \cong 19 \text{ cm}$. The solid curve corresponds to $\kappa_r = 40$ and the dashed curve to $\kappa_r = 10$, each representing a different value of the scaling constant C_r . Note that the predicted scintillation levels for the tracked and untracked beams are basically the same up to ~ 10 – 20 km , but are vastly different (by an order of magnitude or more) at altitudes beyond 20 – 30 km . Atmospheric turbulence is generally assumed to be negligible beyond 20 km .

We show simulation results in Fig. 12.13 as a function of beam size for the uplink longitudinal component of an untracked collimated beam at GEO with

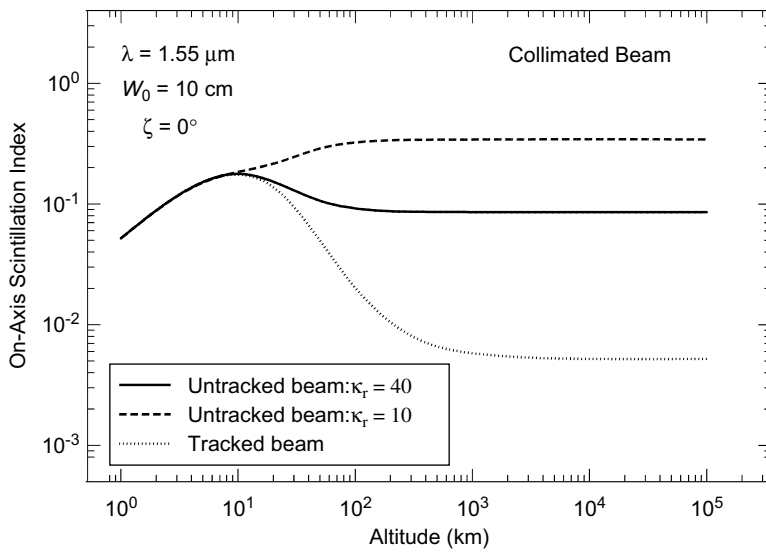


Figure 12.12 Longitudinal scintillation index of a tracked and untracked 10 cm collimated beam as a function of altitude at zero zenith angle.

zenith angles 0 deg and 60 deg. In this example the wavelength is $\lambda = 0.84 \mu\text{m}$, from which we find the spatial coherence radius $r_0 \cong 9 \text{ cm}$ ($\zeta = 0^\circ$) and $r_0 \cong 6 \text{ cm}$ ($\zeta = 60^\circ$). Theoretical curves for untracked beams are shown by

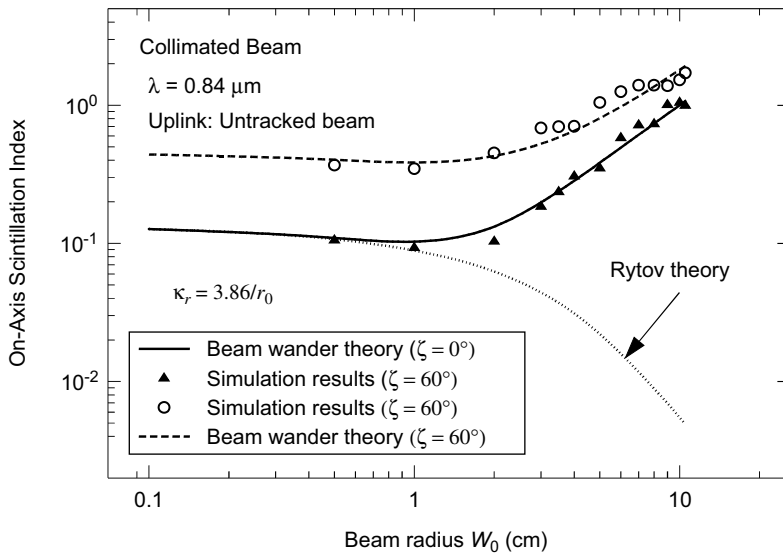


Figure 12.13 The longitudinal component of scintillation as a function of beam radius. The filled triangles and open circles represent simulation results for an untracked beam (courtesy of F. Dios). Theoretical results for untracked beams are also shown as is that based on conventional Rytov theory (dotted curve).

the solid and dashed curves, based on Eq. (54) with $\kappa_r = 3.86/r_0$. For comparison, we also plot the tracked beam theoretical curve for zenith angle zero deduced from Eq. (58). Here we see close agreement of the theoretical model with simulation results for the untracked beam at both featured zenith angles. All results are based on the H-V_{5/7} turbulence model.

12.6.4 Strong fluctuation theory

Under *strong irradiance fluctuations* such as those caused by large-diameter beams and/or large zenith angles we can use the general theory introduced in Chap. 9 for the longitudinal component. For example, in the case of a tracked collimated Gaussian beam, the uplink longitudinal component becomes

$$\begin{aligned} \sigma_I^2(\mathbf{r}, L)_{\text{tracked}} &= 5.95(H - h_0)^2 \sec^2(\zeta) \left(\frac{2W_0}{r_0} \right)^{5/3} \left(\frac{\alpha_r - \sqrt{\langle \alpha_c^2 \rangle}}{W} \right)^2 \\ &\quad \times U\left(\alpha_r - \sqrt{\langle \alpha_c^2 \rangle}\right) + \sigma_{I,l}^2(L)_{\text{tracked}}, \end{aligned} \quad (59)$$

where

$$\begin{aligned} \sigma_{I,l}^2(L)_{\text{tracked}} &= \exp \left[\frac{0.49\sigma_{Bu}^2}{\left(1 + (1 + \Theta)0.56\sigma_{Bu}^{12/5}\right)^{7/6}} + \frac{0.51\sigma_{Bu}^2}{\left(1 + 0.69\sigma_{Bu}^{12/5}\right)^{5/6}} \right] - 1, \\ 0 &\leq \sigma_{Bu}^2 < \infty. \end{aligned} \quad (60)$$

Because the first term on the right-hand side of (59) (i.e., the beam wander term) is based on weak fluctuation theory, the validity of (59) is still subject to the weak fluctuation restriction. However, Eq. (60) is valid under all values of the Rytov parameter (58). For the untracked beam, the corresponding expression is

$$\begin{aligned} \sigma_I^2(\mathbf{r}, L)_{\text{untracked}} &= 5.95(H - h_0)^2 \sec^2(\zeta) \left(\frac{2W_0}{r_0} \right)^{5/3} \left(\frac{\alpha_r - \alpha_{pe}}{W} \right)^2 U(\alpha_r - \alpha_{pe}) \\ &\quad + 5.95(H - h_0)^2 \sec^2(\zeta) \left(\frac{2W_0}{r_0} \right)^{5/3} \left(\frac{\alpha_{pe}}{W} \right)^2 + \sigma_{I,l}^2(L)_{\text{tracked}}. \end{aligned} \quad (61)$$

In Figs. 12.14 and 12.15 we show simulation results of Baker and Benson [23] for an uplink untracked collimated beam to a target at 300 km and zero zenith angle. In Fig. 12.14, we plot the longitudinal component of the scintillation index as a function of beam radius at the transmitter, whereas in Fig. 12.15 we show the scintillation index as a function of off-axis distance for a beam with $W_0 = 5$ cm. Also shown are theoretical results derived from (61) and (59), respectively, with $\kappa_r = \pi/r_0$ and $r_0 = 20$ cm. The dashed curves correspond to conventional Rytov theory. Because $\sigma_{pe} \cong 30$ cm, the (solid) theoretical curve in Fig. 12.15 does not show an increase until $r > \sigma_{pe}$. We show similar simulation

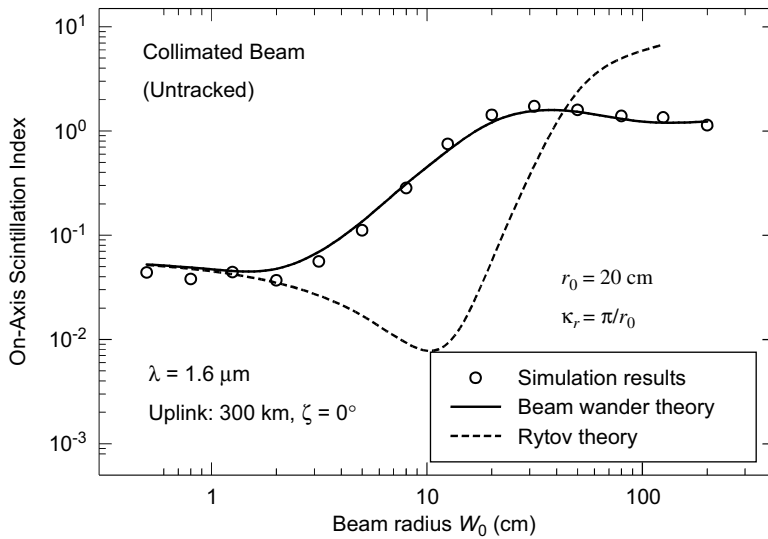


Figure 12.14 On-axis scintillation index for an untracked collimated beam as a function of beam radius at the transmitter. The dashed curve represents conventional Rytov theory. (Simulation results courtesy of G. J. Baker.)

and theoretical results in Figs. 12.16 and 12.17 for the case of a tracked beam. In Fig. 12.16 we plot the on-axis scintillation results of Baker and Benson, and in Fig. 12.17 we plot their simulation results as a function of off-axis radial distance for an initial 5 cm radius beam. Note that there is no appreciable increase

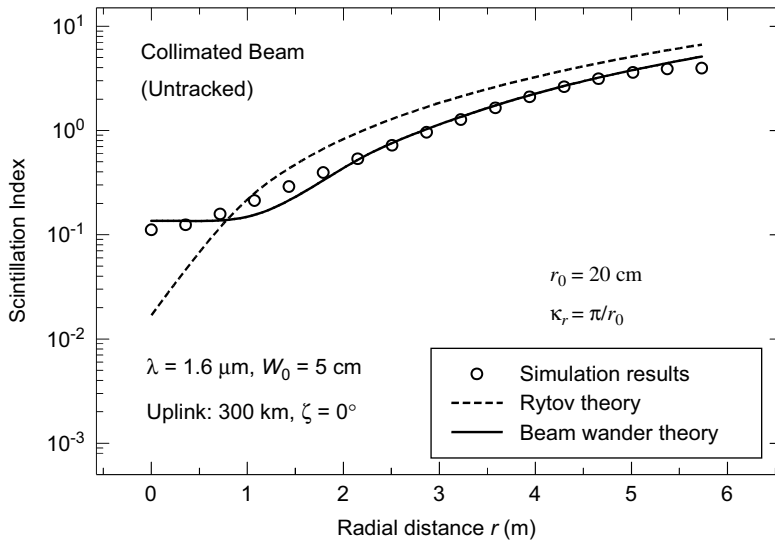


Figure 12.15 Scintillation index for an untracked collimated beam of radius 5 cm as a function of off-axis distance. The dashed curve represents conventional Rytov theory. (Simulation results courtesy of G. J. Baker.)

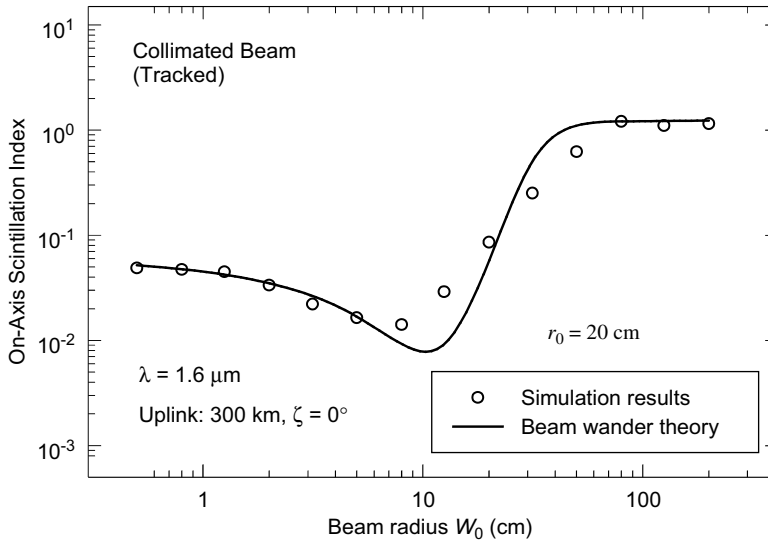


Figure 12.16 On-axis scintillation index for a tracked collimated beam as a function of beam radius at the transmitter. (Simulation results courtesy of G. J. Baker.)

in the theoretical curve or simulation results for the scintillation index until the radial distance exceeds 2 m, i.e., $r > \sqrt{\langle r_c^2 \rangle} \cong 2$ m. For $r > 2$ m the difference between theoretical and simulation results is a consequence of somewhat different tracking schemes.

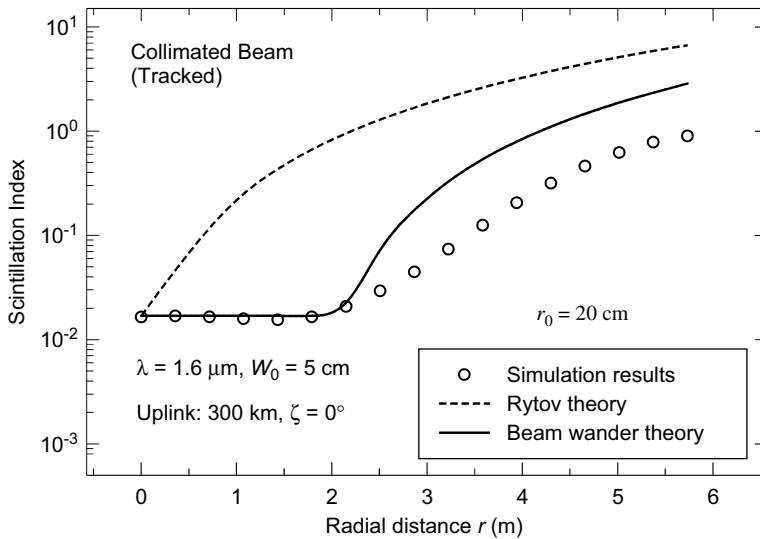


Figure 12.17 Scintillation index for a tracked collimated beam of radius 5 cm as a function of off-axis distance. The dashed curve represents conventional Rytov theory. (Simulation results courtesy of G. J. Baker.)

Last, to more clearly illustrate the change in scintillation index as a function of zenith angle, we choose the limiting case of a *spherical wave* deduced from (60) by setting $\Theta = \Lambda = 0$. However, in this case the quantity σ_{Bu}^2 is defined by [32,33]

$$\sigma_{Bu}^2 = 2.25k^{7/6}(H - h_0)^{5/6} \sec^{11/6}(\zeta) \int_{h_0}^H C_n^2(h) \left(1 - \frac{h - h_0}{H - h_0}\right)^{5/6} \left(\frac{h - h_0}{H - h_0}\right)^{5/6} dh, \quad (62)$$

which represents the scintillation index of a spherical wave under weak irradiance fluctuations. We show the scintillation index in Fig. 12.18 (solid curve) as a function of zenith angle for an uplink spherical wave based on Eqs. (60) and (62). In this example we set wavelength $\lambda = 1.06 \mu\text{m}$ and selected two values of ground level structure constant $C_n^2(0)$. Results based on weak fluctuation theory [as described by (62) alone] are also shown by the dashed curves where we see that weak fluctuation theory is valid only for zenith angles up to roughly 45–60 deg.

12.6.5 Covariance function of irradiance

For an *uplink* path, the corresponding normalized covariance function is

$$b_I(\rho, L) = \frac{B_I(\rho, L)}{B_I(0, L)} = \frac{\mu_{3u}(\rho)}{\mu_{3u}(0)}, \quad (63)$$

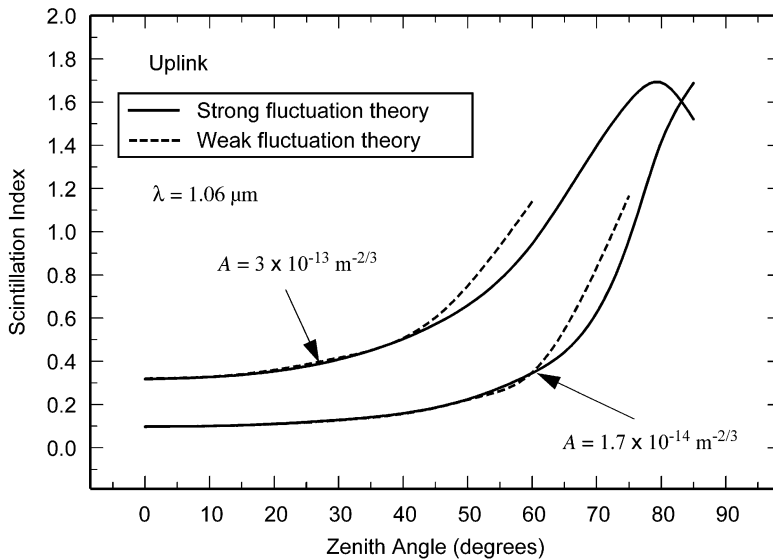


Figure 12.18 Uplink scintillation index of a spherical wave to a satellite receiver as a function of zenith angle and two values of ground level structure constant.

where $\mu_{3u}(0) = \mu_{3u}$ is defined by (55) and

$$\mu_{3u}(\rho) = \mu_{3d}(\rho) \Big|_{\xi=1-(h-h_0)/(H-h_0)}. \quad (64)$$

The implied transverse correlation width for an uplink path deduced from (63) is ordinarily tens of meters or more, far exceeding the probable size of any satellite. Consequently, any size receiver at the satellite always acts like a *point receiver*.

12.7 Fade Statistics: Downlink Channels

In this section we consider a downlink path and examine the effects of atmospheric turbulence on several fade statistical parameters as a function of threshold fade level. Once again, most numerical calculations are based on the H-V_{5/7} atmospheric model.

The reliability of a communication channel due to a laser beam passing through atmospheric turbulence can be deduced from a mathematical model for the probability density function (PDF) of the randomly fading irradiance signal. In the weak fluctuation regime the irradiance statistics of an optical wave are usually assumed to be governed by the *lognormal PDF* model which, for a Gaussian-beam wave, takes the form (see also Section 11.4)

$$\begin{aligned} p_I(I) &= \frac{1}{I\sigma_I(\mathbf{r}, L)\sqrt{2\pi}} \exp \left\{ - \frac{\left[\ln \left(\frac{I}{\langle I(\mathbf{r}, L) \rangle} \right) + \frac{1}{2} \sigma_I^2(\mathbf{r}, L) \right]^2}{2\sigma_I^2(\mathbf{r}, L)} \right\} \\ &= \frac{1}{I\sigma_I(\mathbf{r}, L)\sqrt{2\pi}} \exp \left\{ - \frac{\left[\ln \left(\frac{I}{\langle I(0, L) \rangle} \right) + \frac{2r^2}{W_{LT}^2} + \frac{1}{2} \sigma_I^2(\mathbf{r}, L) \right]^2}{2\sigma_I^2(\mathbf{r}, L)} \right\}, \quad I > 0, \end{aligned} \quad (65)$$

where in the second step we have expressed the mean irradiance in the form

$$\langle I(\mathbf{r}, L) \rangle = \frac{W_0^2}{W_{LT}^2} \exp \left(- \frac{2r^2}{W_{LT}^2} \right) = \langle I(0, L) \rangle \exp \left(- \frac{2r^2}{W_{LT}^2} \right) \quad (66)$$

However, it has been shown that the gamma-gamma distribution may be a more accurate model under weak fluctuation conditions, and it is also valid under moderate-to-strong fluctuations [33,34]. The gamma-gamma PDF is defined by (see Section 9.10)

$$p_I(I) = \frac{2(\alpha\beta)^{(\alpha+\beta)/2}}{\Gamma(\alpha)\Gamma(\beta)I} \left(\frac{I}{\langle I(\mathbf{r}, L) \rangle} \right)^{(\alpha+\beta)/2} K_{\alpha-\beta} \left(2\sqrt{\frac{\alpha\beta I}{\langle I(\mathbf{r}, L) \rangle}} \right), \quad I > 0, \quad (67)$$

where α and β are positive parameters directly related to the large-scale and small-scale scintillations of the optical wave according to

$$\alpha = \left\{ \exp \left[\frac{0.49\sigma_R^2}{\left(1 + 1.11\sigma_R^{12/5}\right)^{7/6}} \right] - 1 \right\}^{-1},$$

$$\beta = \left\{ \exp \left[\frac{0.51\sigma_R^2}{\left(1 + 0.69\sigma_R^{12/5}\right)^{5/6}} \right] - 1 \right\}^{-1}. \quad (68)$$

12.7.1 Fractional fade time

The *fractional fade time* describes the percentage of time the irradiance of the received wave is below some given threshold value I_T . It is customary to express the fade threshold irradiance level I_T below the mean on-axis irradiance in decibels (dB), which is described by the fade threshold parameter

$$F_T = 10 \log_{10} \left(\frac{\langle I(0, L) \rangle}{I_T} \right). \quad [\text{dB}] \quad (69)$$

Here we assume the irradiance fluctuations are an ergodic process where ensemble averages are equal to time averages. Based on the lognormal model (64), the fractional fade time or *probability of miss* (fade) as a function of threshold level becomes the cumulative probability for the irradiance

$$P(I \leq I_T) = \int_0^{I_T} p(I) dI$$

$$= \frac{1}{2} \left\{ 1 + \operatorname{erf} \left[\frac{\frac{1}{2}\sigma_I^2(\mathbf{r}, L) + \frac{2r^2}{W_{LT}^2} - 0.23F_T}{\sqrt{2}\sigma_I(\mathbf{r}, L)} \right] \right\}, \quad (70)$$

where $\operatorname{erf}(x)$ is the error function (see Appendix I) and we have written

$$\ln \left(\frac{I_T}{\langle I(0, L) \rangle} \right) = -0.23F_T. \quad (71)$$

The comparable expression for the cumulative distribution of the gamma-gamma model is given by Eq. (26) in Chap. 11. However, due to numerical difficulties that sometimes occur in computing with the generalized hypergeometric functions owing to the wide range of values the parameters α and β take on, numerical integration of the PDF (67) is generally best for calculating fade probabilities.

The resulting probability of fade for a 4 cm beam based on the lognormal model is plotted in Fig. 12.19 as a function of angular position from the optical

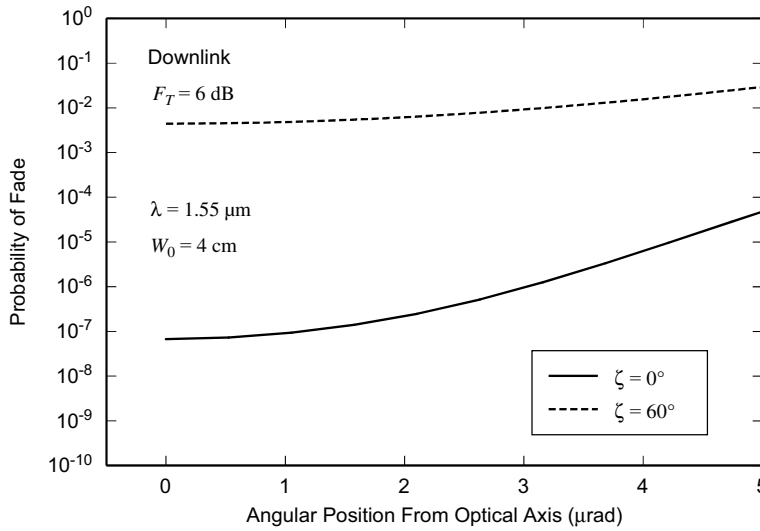


Figure 12.19 Downlink probability of fade as a function of angular receiver position for a collimated beam and lognormal PDF model. The specified fade level below the mean irradiance is $F_T = 6 \text{ dB}$.

axis and zenith angles of 0 and 60 deg. Note that, although the scintillation index is virtually constant across the beam profile, pointing errors are still important for downlink channels because the mean irradiance falls off in the radial direction according to a Gaussian function. In Fig. 12.20 the probability of fade is shown

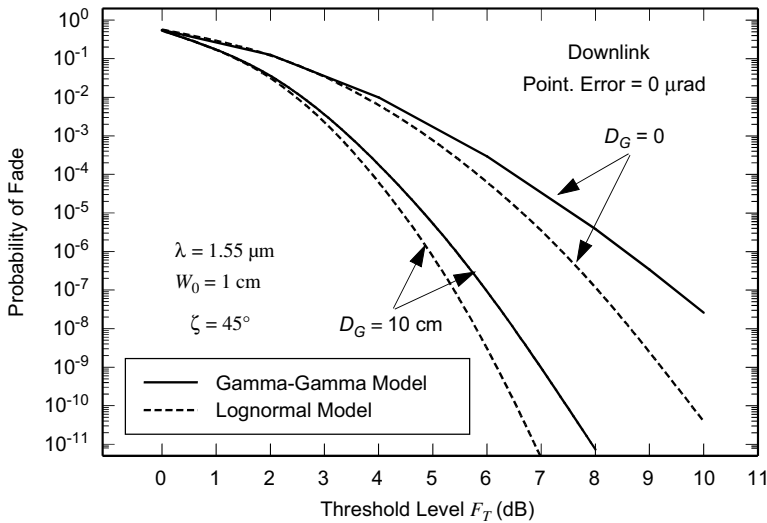


Figure 12.20 Downlink probability of fade as a function of fade threshold level F_T below the mean on-axis irradiance for two receiver aperture sizes. The theoretical curves are based on both the lognormal and gamma-gamma models.

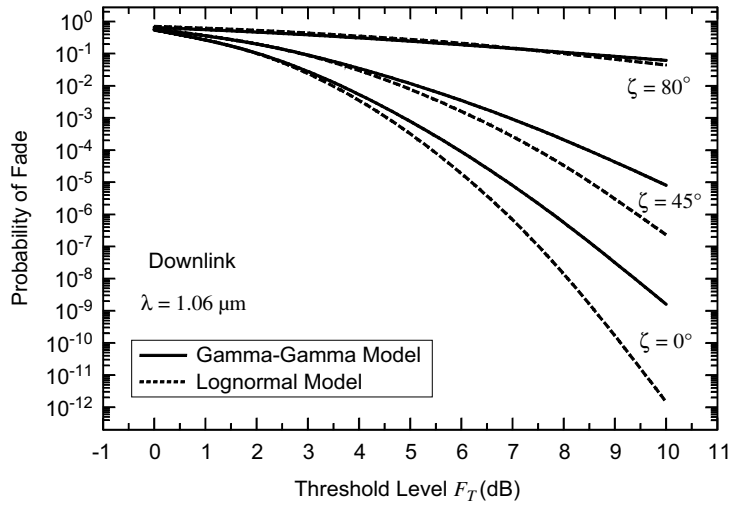


Figure 12.21 Probability of fade as a function of threshold level F_T below the mean irradiance. Results are based on both the gamma-gamma model (solid lines) and the lognormal model (dashed lines).

as a function of fade level F_T (in dB) on the optical axis for both the lognormal and gamma-gamma PDF models and given zenith angle 45 deg. A receiver aperture diameter of 10 cm is compared with a point aperture in this figure to illustrate the effect of aperture averaging. In this case we set $\alpha = [0.49 \sigma_I^2(D_G)]^{-1}$ and $\beta = [0.51 \sigma_I^2(D_G)]^{-1}$, where $\sigma_I^2(D_G)$ is defined by (39). Under a range of zenith angles, the probability of fade based on both the lognormal and gamma-gamma PDF models is illustrated in Fig. 12.21 for the case of a point receiver. The predicted scintillation index throughout the center portion of the beam at the three chosen zenith angles is, respectively, $\sigma_I^2 = 0.10, 0.19$, and 1.07 .

12.7.2 Expected number of fades

The number of negative crossings below a specified irradiance threshold level I_T characterizes the *expected number of fades* per unit time, $\langle n(I_T) \rangle$. This quantity is especially important for acquisition and tracking purposes. For the case of a Gaussian-beam wave and lognormal model, it has been shown that [4,32,33]

$$\langle n(I_T) \rangle = v_0 \exp \left\{ - \frac{\left[\frac{1}{2} \sigma_I^2(\mathbf{r}, L) + \frac{2r^2}{W_{LT}^2} - 0.23 F_T \right]^2}{2 \sigma_I^2(\mathbf{r}, L)} \right\}, \quad (72)$$

where ν_0 is a quasi-frequency defined by the width of the normalized irradiance power spectrum

$$\nu_0 = \frac{1}{2\pi} \left[-\frac{B_I''(0; \mathbf{r}, L)}{B_I(0; \mathbf{r}, L)} \right]^{1/2} = \frac{1}{2\pi} \left[\frac{\int_0^\infty \omega^2 S_I(\omega) d\omega}{\int_0^\infty S_I(\omega) d\omega} \right]^{1/2} \quad (73)$$

The comparable expression for the gamma-gamma PDF has been approximated by [33]

$$\langle n(I_T) \rangle = \frac{2\sqrt{2\pi\alpha\beta}\nu_0\sigma_I}{\Gamma(\alpha)\Gamma(\beta)} \left(\frac{\alpha\beta I_T}{\langle I \rangle} \right)^{(\alpha+\beta-1)/2} K_{\alpha-\beta} \left(2\sqrt{\frac{\alpha\beta I_T}{\langle I \rangle}} \right), \quad (74)$$

where α and β are defined by (68) for a point receiver.

The primes in Eq. (73) denote differentiation with respect to τ of the temporal covariance function $B_I(\tau; \mathbf{r}, L)$ for the irradiance (see Section 8.5). That is, if V_\perp denotes the mean transverse wind speed, then the temporal covariance function for the irradiance of a Gaussian-beam wave propagating from space to ground is given by

$$\begin{aligned} B_I(\tau; \mathbf{r}, L) &= 8\pi^2 k^2 \sec(\zeta) \int_{h_0}^H \int_0^\infty \kappa \Phi_n(\kappa, h) J_0(\kappa V_\perp \tau) \exp\left(-\frac{\Lambda L \kappa^2 \xi^2}{k}\right) \\ &\quad \times \left\{ I_0(2\Lambda \kappa r \xi) - \cos\left[\frac{L \kappa^2}{k} \xi(1 - \bar{\Theta}\xi)\right] \right\} d\kappa dh \\ &\cong 8\pi^2 k^2 \sec(\zeta) \int_{h_0}^H \int_0^\infty \kappa \Phi_n(\kappa, h) J_0(\kappa V_\perp \tau) \\ &\quad \times \left[1 - \cos\left(\frac{L \kappa^2 \xi}{k}\right) \right] d\kappa dh, \end{aligned} \quad (75)$$

the last step of which has been approximated by that of a plane wave. The second derivative of (75) evaluated at $\tau = 0$ leads to

$$B_I''(0; L) \cong -3.503 k^{7/6} \mu_{5d} (H - h_0)^{5/6} \sec^{11/6}(\zeta) \left(\frac{k V_\perp^2}{L} \right), \quad (76)$$

where we have ignored the radial dependence in this case and

$$\mu_{5d} = \int_{h_0}^H C_n^2(h) \left(\frac{H - h_0}{h - h_0} \right)^{1/6} dh. \quad (77)$$

The expected number of fades for a downlink channel is shown in Fig. 12.22 for the same conditions as described in Fig. 12.20. In this case we set the quasi-frequency at 550 Hz.

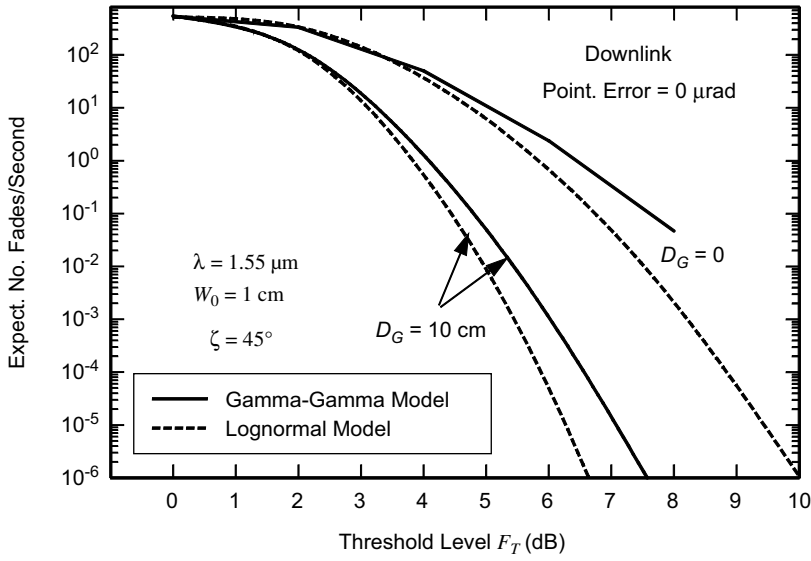


Figure 12.22 Downlink expected number of fades per second plotted as a function of fade level F_T below the mean on-axis irradiance for two receiver aperture sizes.

12.7.3 Mean fade time

When the irradiance of the beam fades below a given level I_T the average time at which it stays below this level defines the *mean duration of fade time* (in seconds), which is determined from the expression

$$\langle t(F_T) \rangle = \frac{P_I(I \leq I_T)}{\langle n(I_T) \rangle}, \quad (78)$$

where $P_I(I \leq I_T)$ represents the cumulative time the irradiance stays below the level I_T and $\langle n(I_T) \rangle$ is the corresponding average number of crossings per unit time. In the case of a lognormal channel, this becomes

$$\begin{aligned} \langle t(F_T) \rangle = \frac{1}{2v_0} \exp \left\{ \frac{\left[\frac{1}{2} \sigma_I^2(\mathbf{r}, L) + \frac{2r^2}{W_{LT}^2} - 0.23F_T \right]^2}{2\sigma_I^2(\mathbf{r}, L)} \right\} \\ \times \left[1 + \operatorname{erf} \left\{ \frac{\left[\frac{1}{2} \sigma_I^2(\mathbf{r}, L) + \frac{2r^2}{W_{LT}^2} - 0.23F_T \right]}{\sqrt{2}\sigma_I(\mathbf{r}, L)} \right\} \right]. \end{aligned} \quad (79)$$

For a space-to-ground communication channel, the mean duration of a fade (in seconds) is shown in Fig. 12.23 for the same conditions as those cited in Figs. 12.20 and 12.22. Here we can see that, although increasing the fade threshold

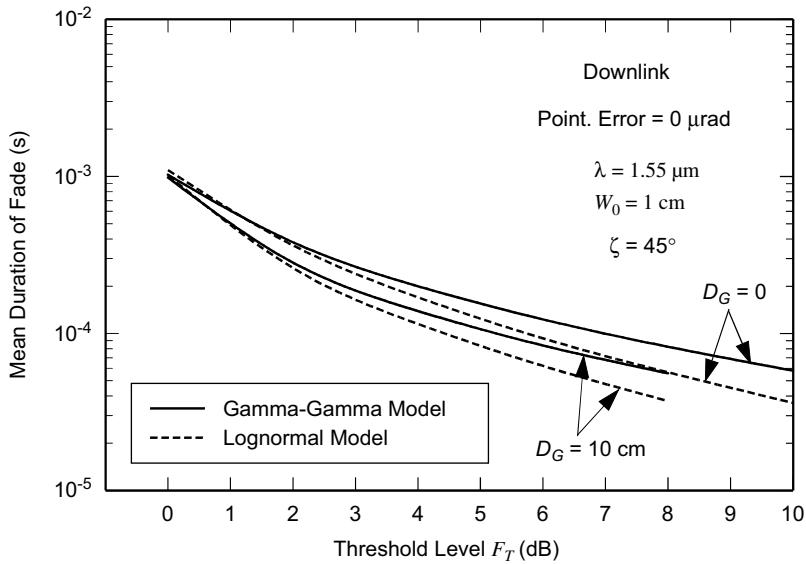


Figure 12.23 Downlink mean duration of a fade plotted as a function of fade level F_T below the mean on-axis irradiance for two receiver aperture sizes.

level F_T to more than a few dB below the mean value can substantially reduce the expected number of fades per unit time, it does not decrease the mean duration of such fades by an appreciable amount. For data rates greater than 10 kb/s, these fades can result in long strings of erroneous bits or unrealistic high error probabilities.

12.8 Fade Statistics: Uplink Channels

The fade statistics of interest for uplink communication channels are essentially the same as for downlink channels. However, for ground-to-space propagation paths the beam wander problem has to be addressed for tracked and untracked beams. Again, all calculations are based on the H- $V_{5/7}$ atmospheric model.

12.8.1 Gamma-gamma distribution

Because of beam wander effects, the scintillation characteristics of an uplink collimated beam are very different from that predicted by conventional Rytov theory, particularly for intermediate-size beams in which $W_0 \sim r_0$. Thus, the gamma-gamma PDF will take on different shapes depending on the transmitted beam size.

To define the parameters of the gamma-gamma PDF, we associate the pointing error term in the longitudinal component of the uplink scintillation

index with the large-scale fluctuations. Therefore, we set $\alpha = 1/\sigma_X^2$ and $\beta = 1/\sigma_Y^2$, where

$$\sigma_X^2 = 5.95(H - h_0)^2 \sec^2(\zeta) \left(\frac{2W_0}{r_0} \right)^{5/3} \left(\frac{\alpha_{pe}}{W} \right)^2 + \exp \left[\frac{0.49\sigma_{Bu}^2}{\left(1 + (1 + \Theta)0.56\sigma_{Bu}^{12/5} \right)^{7/6}} \right] - 1, \quad (80)$$

$$\sigma_Y^2 = \exp \left[\frac{0.51\sigma_{Bu}^2}{\left(1 + 0.69\sigma_{Bu}^{12/5} \right)^{5/6}} \right] - 1. \quad (81)$$

In Fig. 12.24 we plot the corresponding gamma-gamma PDF for three different beam sizes corresponding to 1, 10, and 50 cm radii. Once again, we set $\lambda = 1.55 \mu\text{m}$ and assume a satellite at GEO. Typical of small beams in which $2W_0/r_0 \ll 1$, the longitudinal component of the scintillation index will generally be much less than unity and the corresponding PDF will have a shape similar to that of a lognormal model, except in the extreme tails. However, for large beams in which $2W_0/r_0 \gg 1$ the scintillation index will move toward saturation and the behavior of the PDF will then approach that of a negative exponential distribution, characteristic of saturated scintillation.

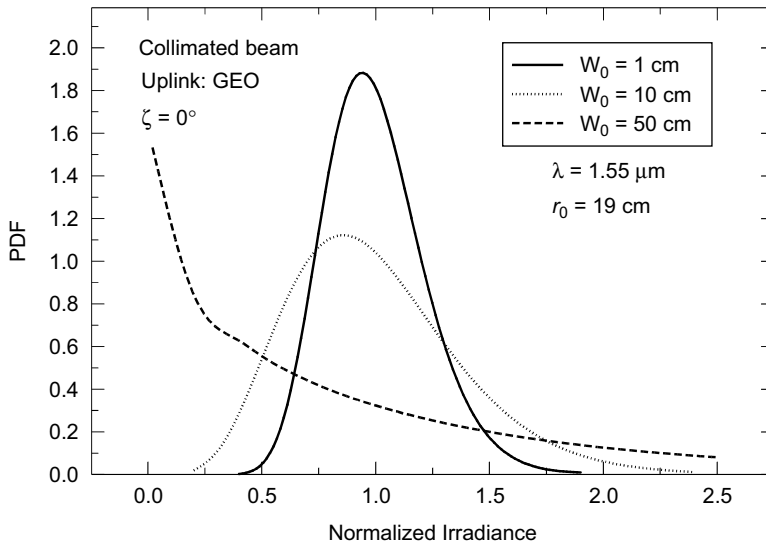


Figure 12.24 Gamma-gamma distribution for an untracked collimated beam plotted as a function of the normalized irradiance for an uplink channel at zero degrees zenith.

12.8.2 Fractional fade time

The *probability of fade* models based on the lognormal and gamma-gamma PDFs for an uplink path are the same as those for the downlink path, except the uplink mean irradiance and scintillation index must be used. Before examining fade statistics for an uplink collimated beam, it may be instructive to first consider the limiting case of a spherical wave.

In Fig. 12.25 the probability of fade for an uplink spherical wave operating at wavelength $\lambda = 1.06 \mu\text{m}$ is shown as a function of fade threshold level F_T (in dB) below the mean irradiance for a satellite in geostationary orbit at various zenith angles ($\zeta = 0, 45$, and 80 deg). The predicted scintillation index at a satellite at these various zenith angles is $\sigma_I^2 = 0.11, 0.20$, and 1.45 , respectively, the latter corresponding to moderate-to-strong irradiance fluctuations. Both the lognormal and gamma-gamma PDF models are featured in this figure for the purpose of comparison. We can see that in general the lognormal model predicts a lower probability of fade as compared with that of the gamma-gamma model. Similar fade probability curves for a Gaussian-beam wave will depend on whether the beam is tracked or not, using the scintillation models developed in Section 12.6.

In Fig. 12.26 we show the probability of fade for a collimated beam as a function of threshold level F_T (in dB) below the mean irradiance for a satellite in geostationary orbit. The beam radius at the transmitter is 10 cm and the wavelength is $1.55 \mu\text{m}$. Both tracked and untracked beam fade probabilities are illustrated at zenith angles of 0 deg and 45 deg. Here we can clearly see a

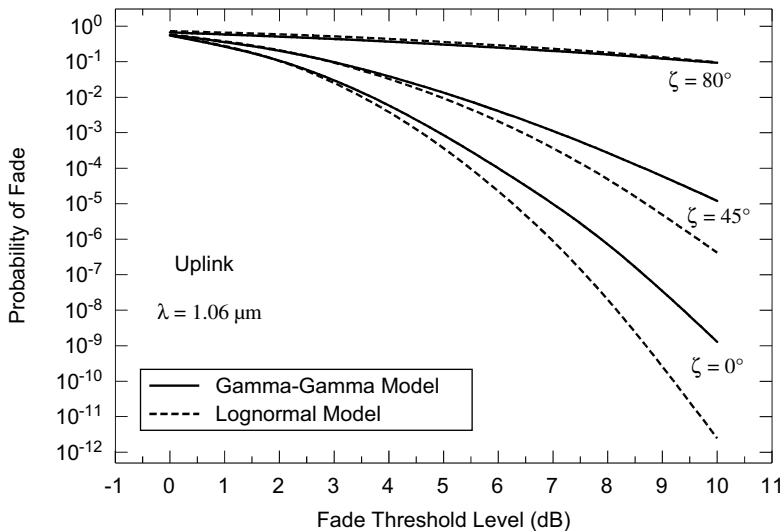


Figure 12.25 Probability of fade as a function of threshold level F_T below the mean irradiance and various zenith angles. Results are for a spherical wave based on both the gamma-gamma and lognormal models.

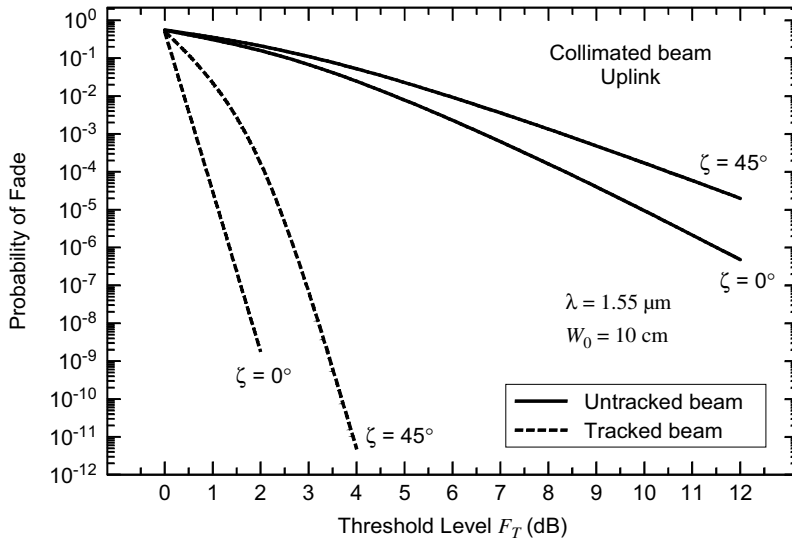


Figure 12.26 Probability of fade as a function of threshold level F_T below the mean irradiance. Results are for both tracked and untracked collimated beams at two zenith angles based on a gamma-gamma PDF.

significant difference in fade probabilities depending on whether the beam is tracked³ or not.

12.8.3 Expected number of fades

For the lognormal model, the *expected number of fades* per unit time is defined by Eq. (72), using uplink results for the mean irradiance and scintillation index. In the case of the gamma-gamma PDF, the comparable expression is that defined by Eq. (74). For calculating the quasi-frequency ν_0 , the second derivative of the temporal covariance function for an uplink path is

$$B_I''(0; \mathbf{r}, L) = -3.63k^{7/6}(H - h_0)^{5/6} \sec^{11/6}(\zeta) \left(\frac{kV_{\perp}^2}{L} \right) \left(\mu_{5u} + \frac{\mu_{4u}}{3\Lambda^{1/6}} \frac{r^2}{W^2} \right), \quad (82)$$

where

$$\mu_{4u} = \int_{h_0}^H C_n^2(h) \left(1 - \frac{h - h_0}{H - h_0} \right)^{-1/3} dh, \quad (83)$$

$$\mu_{5u} = \text{Re} \int_{h_0}^H C_n^2(h) \left\{ \frac{1}{\Lambda^{1/6} \xi^{1/3}} - \frac{1}{\xi^{1/6} [\Lambda \xi + i(1 - \Theta \xi)]^{1/6}} \right\} dh, \quad (84)$$

and where $\xi = 1 - (h - h_0)/(H - h_0)$.

³The gamma-gamma PDF is only an approximation for the untracked beam case.

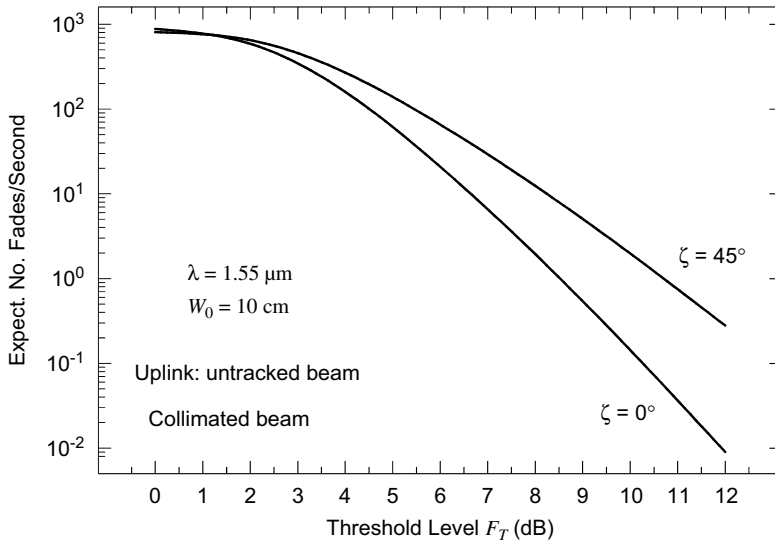


Figure 12.27 Uplink expected number of fades per second for a collimated beam at two zenith angles and plotted as a function of fade level F_T below the mean on-axis irradiance.

The expected number of fades for an uplink channel can be deduced from (74) where the parameters α and β are defined by $\alpha = 1/\sigma_X^2$ and $\beta = 1/\sigma_Y^2$, and the large- and small-scale irradiance fluctuations are given by (80) and (81), respectively. In Fig. 12.27 we show the expected number of fades per second as a function of fade level F_T below the mean irradiance for the same untracked collimated beam illustrated in Fig. 12.26 at zenith angles 0 deg and 45 deg. For illustrative purposes we set the quasi-frequency at the nominal value of $\nu_0 = 550$ Hz. Because the quasi-frequency is a multiplicative constant, the expected number of fades/second for other quasi-frequencies can be readily determined from these curves.

12.8.4 Mean fade time

Knowledge of the probability of fade and the expected number of fades per second permits an easy calculation of the mean duration of fade or *mean fade time* by use of (78). By once again using the gamma-gamma PDF, we show the mean fade time in Fig. 12.28 as a function of fade level F_T below the mean irradiance for the same untracked collimated beam as illustrated in Figs. 12.26 and 12.27.

12.9 Summary and Discussion

In this chapter we have presented an overview of some of the atmospheric effects that are of importance in the design of any satellite communication system.

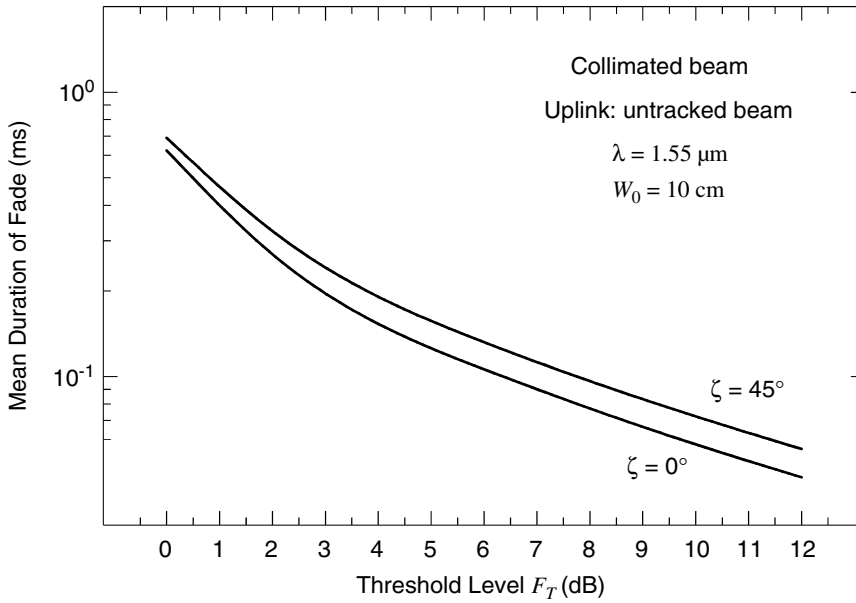


Figure 12.28 Uplink mean duration of fade for a collimated beam at two zenith angles and plotted as a function of fade threshold level F_T below the mean irradiance.

The detailed analysis and numerical results presented here are based on the H-V_{5/7} profile model for C_n^2 . Although this particular atmospheric model is likely the most widely used model for such calculations, it does not permit sufficient flexibility to represent all probable locations of laser transmitters nor take into account the non-isotropic nature of the stratosphere. Nonetheless, the numerical predictions based on this model give some indication of the beam statistics associated with satellite communication systems and, moreover, the analytic expressions are valid for other C_n^2 profile models.

Using mostly weak fluctuation theory, expressions are provided here for calculating the mean irradiance, scintillation index, fractional fade time, expected number of fades, and mean duration of fade time for both downlink and uplink channels of a laser satellite communication system. Weak fluctuation theory is restricted to pointing errors less than a few microradians and/or zenith angles not exceeding 45–60 deg for a ground-based transmitter/receiver. The equations also include the geometry parameters for links between a satellite and either a ground-based or airborne-based transmitter/receiver.

Downlink channel:

On a downlink channel, the following is a list of primary parameters that are generally evaluated numerically using a suitable profile model for the refractive-index structure parameter $C_n^2(h)$:

$$\mu_0 = \int_{h_0}^H C_n^2(h) dh \quad (85)$$

$$\mu_{1d} = \int_{h_0}^H C_n^2(h) \left[\Theta + \overline{\Theta} \left(\frac{h - h_0}{H - h_0} \right) \right]^{5/3} dh \quad (86)$$

$$\mu_{2d} = \int_{h_0}^H C_n^2(h) \left(\frac{h - h_0}{H - h_0} \right)^{5/3} dh \quad (87)$$

$$\begin{aligned} \mu_{3d} &= \text{Re} \int_{h_0}^H C_n^2(h) \left\{ \xi^{5/6} [\Lambda \xi + i(1 - \overline{\Theta} \xi)]^{5/6} - \Lambda^{5/6} \xi^{5/3} \right\} dh \\ &\cong 0.26 \int_{h_0}^H C_n^2(h) \left(\frac{h - h_0}{H - h_0} \right)^{5/6} dh \end{aligned} \quad (88)$$

where $\xi = (h - h_0)/(H - h_0)$

In terms of these parameters, we then calculate:

Spatial coherence radius:

$$\begin{aligned} \rho_0 &= (1.45 \mu_0 k^2)^{-3/5} \cos^{3/5}(\zeta) \\ r_0 &= 2.1 \rho_0 \end{aligned} \quad (89)$$

RMS angle of arrival:

$$\langle \beta_a^2 \rangle^{1/2} = [2.91 \mu_0 (2W_G)^{-1/3} \sec(\zeta)]^{1/2} \quad (90)$$

Effective spot size:

$$W_{LT} \cong W \quad (91)$$

Scintillation index (weak fluctuations):

$$\sigma_I^2(\mathbf{r}, L) \cong \sigma_R^2 = 8.70 \mu_{3d} k^{7/6} (H - h_0)^{5/6} \sec^{11/6}(\zeta), \quad \sigma_R^2 < 1 \quad (92)$$

Scintillation index (weak-strong fluctuations):

$$\begin{aligned} \sigma_I^2(0, L) &= \exp \left[\frac{0.49 \sigma_R^2}{\left(1 + 1.11 \sigma_R^{12/5} \right)^{7/6}} + \frac{0.51 \sigma_R^2}{\left(1 + 0.69 \sigma_R^{12/5} \right)^{5/6}} \right] - 1, \\ 0 &\leq \sigma_R^2 < \infty \end{aligned} \quad (93)$$

Downlink Channel Summary:

Beam spreading is mostly confined to pure diffraction.

Off-axis scintillations remain essentially constant across the beam profile at the receiver and are independent of the initial beam size. The scintillation index is approximately that of an infinite plane wave.

Pointing errors increase the probability of fade because of the Gaussian-beam profile for the mean irradiance.

The irradiance correlation width at the ground is usually only several centimeters. Thus, aperture averaging will occur for sufficiently large receiver apertures.

The rms angle-of-arrival fluctuations are on the order of several microradians.

Beam wander does not occur for downlink channels.

The use of multiple coherent detection receivers (sufficiently separated) can significantly reduce the probability of fade and the expected number of fades [35].

Uplink Channel:

For an uplink channel, the parameters that are numerically evaluated using a profile model for the refractive-index structure parameter $C_n^2(h)$ are the following:

$$\mu_{1u} = \int_{h_0}^H C_n^2(h) \left[\Theta + \overline{\Theta} \left(\frac{h - h_0}{H - h_0} \right) \right]^{5/3} dh \quad (94)$$

$$\mu_{2u} = \int_{h_0}^H C_n^2(h) \left(1 - \frac{h - h_0}{H - h_0} \right)^{5/3} dh \quad (95)$$

$$\mu_{3u} = \text{Re} \int_{h_0}^H C_n^2(h) \left\{ \xi^{5/6} [\Lambda \xi + i(1 - \overline{\Theta} \xi)]^{5/6} - \Lambda^{5/6} \xi^{5/3} \right\} dh \quad (96)$$

where $\xi = 1 - (h - h_0)/(H - h_0)$

In terms of these parameters, we can calculate the following statistics:

Effective spot size:

$$W_{LT} = W \sqrt{1 + 4.35 \mu_{2u} \Lambda^{5/6} k^{7/6} (H - h_0)^{5/6} \sec^{11/6}(\zeta)} \quad (\text{weak}) \quad (97)$$

or

$$W_{LT} = \begin{cases} W \sqrt{1 + (D_0/r_0)^{5/3}}, & 0 \leq D_0/r_0 < 1 \\ W [1 + (D_0/r_0)^{5/3}]^{3/5}, & 0 \leq D_0/r_0 < \infty \end{cases}$$

rms beam wander ($\kappa_0 = 0$):

$$\sqrt{\langle r_c^2 \rangle} = 0.73 (H - h_0) \sec(\zeta) \left(\frac{\lambda}{2W_0} \right) \left(\frac{2W_0}{r_0} \right)^{5/6} \quad (98)$$

On-axis scintillation index (tracked):

$$\sigma_{I,I}^2(L)_{\text{tracked}} = \exp \left[\frac{0.49\sigma_{Bu}^2}{\left(1 + 0.56(1 + \Theta)\sigma_{Bu}^{12/5}\right)^{7/6}} + \frac{0.51\sigma_{Bu}^2}{\left(1 + 0.69\sigma_{Bu}^{12/5}\right)^{5/6}} \right] - 1$$

$$\sigma_{Bu}^2 = 8.70 \mu_{3u} k^{7/6} (H - h_0)^{5/6} \sec^{11/6}(\zeta), \quad 0 \leq \sigma_{Bu}^2 < \infty \quad (99)$$

On-axis scintillation index (untracked):

$$\sigma_{I,I}^2(L)_{\text{untracked}} = 5.95(H - h_0)^2 \sec^2(\zeta) \left(\frac{2W_0}{r_0} \right)^{5/3} \left(\frac{\alpha_{pe}}{W} \right)^2$$

$$+ \exp \left[\frac{0.49\sigma_{Bu}^2}{\left(1 + (1 + \Theta)0.56\sigma_{Bu}^{12/5}\right)^{7/6}} + \frac{0.51\sigma_{Bu}^2}{\left(1 + 0.69\sigma_{Bu}^{12/5}\right)^{5/6}} \right] - 1$$

(100)

Uplink Channel Summary:

Small pointing errors (several microradians) can cause serious degradation in the communication channel reliability because of off-axis scintillation. Moreover, off-axis scintillation can approach saturation very rapidly in the radial direction for larger beam diameters. Smaller beams have less off-axis scintillation, thereby reducing the pointing error requirement.

The irradiance correlation width at the satellite is many times larger than the probable size of the satellite so that any receiver at the satellite always behaves like a point receiver.

The rms value of the angle-of-arrival fluctuations at the satellite is generally less than 1 μrad .

Beam wander at the satellite can be as large as several microradians. However, beam wander can be mitigated by the use of multiple beams or a fast-tracking transmitter.

12.10 Worked Examples

Example 1: Consider an uplink propagation path to a satellite in geostationary orbit. If the input parameters for a collimated beam at the transmitter are $\lambda = 1.06 \mu\text{m}$, $W_0 = 2 \text{ cm}$, $h_0 = 0$, and $\zeta = 30^\circ$, determine the following beam characteristics at the satellite:

- (a) diffraction-limited beam radius,
- (b) effective beam radius,

- (c) scintillation index on the optical axis for tracked and untracked beams, and
- (d) rms beam wander.

Solution: For a geostationary orbit we set $H = 38.5 \times 10^3$ km. Also, for the H-V_{5/7} model for $C_n^2(h)$, we set $A = 1.7 \times 10^{-14} \text{ m}^{-2/3}$ and $w = 21 \text{ m/s}$. We first numerically calculate the following parameters:

$$\Theta_0 = 1 - \frac{L}{F_0} = 1, \quad \Lambda_0 = \frac{2L}{kW_0^2} = 37,500$$

$$\Theta = \frac{\Theta_0}{\Theta_0^2 + \Lambda_0^2} = 7.11 \times 10^{-10}, \quad \Lambda = \frac{\Lambda_0}{\Theta_0^2 + \Lambda_0^2} = 2.67 \times 10^{-5},$$

$$\mu_0 = 2.24 \times 10^{-12} \text{ m}^{1/3}, \quad \mu_{3u} = 3.70 \times 10^{-17} \text{ m}^{1/3}, \quad r_0 = 11.24 \text{ cm}.$$

- (a) $W = 750 \text{ m}$ ($16.9 \text{ } \mu\text{rad}$),
- (b) $W_{LT} = 864 \text{ m}$ ($19.4 \text{ } \mu\text{rad}$),
- (c) $\sigma_I^2 = 0.07$ (tracked), $\sigma_I^2 = 0.095$ (untracked),
- (d) $\langle r_c^2 \rangle^{1/2} = 369 \text{ m}$ ($8.3 \text{ } \mu\text{rad}$).

□

Example 2: Consider a downlink propagation path from a satellite in geostationary orbit to a ground receiver station. If the input parameters for a collimated beam at the transmitter are $\lambda = 1.06 \text{ } \mu\text{m}$, $W_0 = 2 \text{ cm}$, and $\zeta = 30 \text{ deg}$, determine the following beam characteristics at the ground station:

- (a) diffraction-limited beam radius,
- (b) effective beam radius,
- (c) scintillation index on the optical axis ($\alpha_r = 0$) and off-axis at $\alpha_r = 5 \text{ } \mu\text{rad}$,
- (d) spatial coherence radius,
- (e) isoplanatic angle.

Solution: For a geostationary orbit we set $H = 38.5 \times 10^3$ km. Also, for the H-V_{5/7} model for $C_n^2(h)$, we set $A = 1.7 \times 10^{-14} \text{ m}^{-2/3}$ and $w = 21 \text{ m/s}$. The Gaussian beam parameters in this case are the same as those given in Example 1. The numerical calculation of the parameters based on Eqs. (21), (78), and (79) leads to:

$$\mu_0 = 2.24 \times 10^{-12} \text{ m}^{1/3}, \quad \mu_{1d} = 1.98 \times 10^{-19} \text{ m}^{1/3}, \quad \mu_{2d} = 6.74 \times 10^{-17} \text{ m}^{1/3}.$$

- (a) $W = 750 \text{ m}$ ($16.9 \text{ } \mu\text{rad}$),
- (b) $W_{LT} = 750 \text{ m}$ ($16.9 \text{ } \mu\text{rad}$),
- (c) $\sigma_I^2 = 0.13$ (on-axis), $\sigma_I^2 = 0.13$ (off-axis at $\alpha_r = 5 \text{ } \mu\text{rad}$),
- (d) $\rho_0 = 5.35 \text{ cm}$,
- (e) $\theta_0 = 13.5 \text{ } \mu\text{rad}$.

□

Problems

Section 12.4

1. For a point source on the ground, show that the uplink WSF (16) can be expressed as

$$D(\rho, L) = 2.914k^2\rho^{5/3} \sec(\zeta) \int_0^H C_n^2(h)(h/H)^{5/3} dh.$$

2. Given that $\mu_0 = 2.24 \times 10^{-12} \text{ m}^{1/3}$ for the H-V_{5/7} model and $H \gg 20 \text{ km}$, what is the implied atmospheric coherence width r_0 for a downlink path with the receiver on the ground, zenith angle $\zeta = 0$, and wavelength
 - (a) $\lambda = 1.06 \text{ }\mu\text{m}$?
 - (b) $\lambda = 0.5 \text{ }\mu\text{m}$?
 Hint: Recall that $r_0 = 2.1\rho_0$.
3. Given that $\mu_0 = 2.24 \times 10^{-12} \text{ m}^{1/3}$ for the H-V_{5/7} model and $H \gg 20 \text{ km}$, what is the rms angle of arrival for a downlink path with zenith angle $\zeta = 0$ and receiver diameter
 - (a) 1 cm?
 - (b) 10 cm?
4. For the special case of a spherical wave and $\lambda = 1.55 \text{ }\mu\text{m}$, calculate the isoplanatic angle given zenith angle
 - (a) $\zeta = 0 \text{ deg}$
 - (b) $\zeta = 60 \text{ deg}$
 - (c) If $\lambda = 0.5 \text{ }\mu\text{m}$ and the zenith angle is zero, what is the resulting isoplanatic angle?

Section 12.5

5. If we define $T = -2E_1(0, 0) - E_2(0, 0)$, the long-term spot size of the beam can be expressed as

$$W_{LT} = W\sqrt{1 + T}.$$

To evaluate the parameter T , we can use the limit

$$T = \lim_{\varepsilon \rightarrow 0^+} \left[4\pi^2 k^2 \sec(\zeta) \int_{h_0}^H \int_0^\infty \kappa \Phi_n(\kappa, h) e^{-\varepsilon \kappa^2} \left(1 - e^{-\Lambda L \kappa^2 \xi^2 / k} \right) d\kappa dh \right],$$

where we have introduced the exponential function $e^{-\varepsilon \kappa^2}$ to aid in the convergence of the integrals. By use of the Kolmogorov spectrum, expand $1 - \exp(\Lambda L \kappa^2 \xi^2 / k)$ in a power series and evaluate the inside integral through termwise integration, thus showing that for a downlink path:

$$T = 4.35 \mu_{2d} \Lambda^{5/6} k^{7/6} (H - h_0)^{5/6} \sec^{11/6}(\zeta).$$

Hint: Use (GH2) in Appendix I.

6. Show that evaluation of the integrals in (35) leads to the expression for the downlink scintillation index given by

$$\sigma_I^2(\mathbf{r}, L) = 8.702k^{7/6}(H - h_0)^{5/6} \sec^{11/6}(\zeta) \times \left[\mu_{3d} + 1.67 \frac{\mu_{2d} \Lambda^{5/6} \alpha_r^2 (H - h_0)^2 \sec^2(\zeta)}{W_0^2 (\Theta_0^2 + \Lambda_0^2)} \right], \quad \alpha_r \leq W/L,$$

where $\alpha_r = r/L$ is the angle in radians that defines the radial distance from the optical axis of the beam (i.e., the pointing error).

7. For the case of an infinite plane wave, show that the result in Prob. 6 reduces to

$$\sigma_I^2(L) = 2.25k^{7/6} \sec^{11/6}(\zeta) \int_{h_0}^H C_n^2(h)(h - h_0)^{5/6} dh.$$

Section 12.6

8. Use the technique in Prob. 5 to deduce that the long-term spot size for an uplink path can be written as

$$W_{LT} = W \sqrt{1 + 4.35 \mu_{2u} \Lambda^{5/6} k^{7/6} (H - h_0)^{5/6} \sec^{11/6}(\zeta)}.$$

9. Use the principle of reciprocity to show that the long-term spot radius in Prob. 9 can also be written as

$$W_{LT} = W \sqrt{1 + (D_0/r_0)^{5/3}}, \quad D_0^2 = 8W_0^2.$$

10. Given that $\mu_0 = 2.24 \times 10^{-12} \text{ m}^{1/3}$ for the H-V_{5/7} model and a GEO satellite, what is the rms beam wander displacement on an uplink path, assuming an infinite outer scale, a 10 cm radius collimated beam operating at $\lambda = 1.55 \text{ } \mu\text{m}$, and zenith angle

- (a) $\zeta = 0 \text{ deg}$
 (b) $\zeta = 60 \text{ deg}$
 (c) What is the rms movement if $\lambda = 0.5 \text{ } \mu\text{m}$? Explain.

11. If the transmitted wave on an uplink path is a spherical wave,
 (a) show that the scintillation index (58) reduces to

$$\sigma_I^2(L) = 2.25k^{7/6} \sec^{11/6}(\zeta) \int_{h_0}^H C_n^2(h)(h - h_0)^{5/6} \left(1 - \frac{h - h_0}{H - h_0}\right)^{5/6} dh.$$

- (b) For a ground-based transmitter, justify the reduction of the result in part (a) to

$$\sigma_I^2(L) \cong 2.25k^{7/6} \sec^{11/6}(\zeta) \int_0^H C_n^2(h)h^{5/6} dh.$$

12. Consider an uplink propagation path to a satellite in GEO. If the input parameters for a collimated beam at the transmitter are $\lambda = 1.55 \mu\text{m}$, $W_0 = 20 \text{ cm}$, $h_0 = 0$, and $\zeta = 45 \text{ deg}$ determine the following beam characteristics at the satellite:
- (a) diffraction-limited beam radius,
 - (b) long-term beam radius,
 - (c) scintillation index on the optical axis for tracked and untracked beams, and
 - (d) rms beam wander.

Section 12.7

13. Starting with Eq. (65) for the lognormal irradiance PDF, derive the fractional fade time expression given by Eq. (70).
14. For the case of a Gaussian-beam wave, show that

$$\langle \ln[I(\mathbf{r}, L)] \rangle = \ln \langle I(\mathbf{r}, L) \rangle - \frac{1}{2} \sigma_I^2(\mathbf{r}, L).$$

15. Use the lognormal model to calculate the probability of fade (dashed) curves shown in Fig. 12.20 for a 10 cm beam radius with $\lambda = 1.55 \mu\text{m}$.

Section 12.8

16. Consider an uplink spherical wave from ground level with $\lambda = 1.55 \mu\text{m}$ and zenith angle 45 deg . Use Eqs. (80) and (81) to calculate the large-scale and small-scale fluctuations of the received optical wave at a satellite in GEO.
17. Use the lognormal model and wavelength $\lambda = 0.84 \mu\text{m}$ to determine the probability of fade curves (dashed) shown in Fig. 12.25.
18. Repeat Prob. 17 for the case where the transmitter is located on an aircraft flying at an altitude of 10 km. (Neglect movement of the aircraft.)
19. Use the gamma-gamma distribution to calculate the probability of fade of an untracked uplink 20 cm radius collimated beam with wavelength $\lambda = 1.55 \mu\text{m}$. Assume the receiver is on a satellite in GEO at the center of the beam and
- (a) $\zeta = 0 \text{ deg}$.
 - (b) $\zeta = 45 \text{ deg}$.
20. Repeat Prob. 19 for the lognormal model.

References

1. B. L. Edelson and G. Hyde, "A Report of the IEEE-USA Aerospace Policy Committee on Laser Satellite Communications, Programs, Technology and Applications" (April 1996).
2. W. B. Miller, J. C. Ricklin, and L. C. Andrews, "Effects of the refractive index spectral model on the irradiance variance of a Gaussian beam," *J. Opt. Soc. Am. A* **11**, 2719–2726 (1994).
3. P. A. Lightsey, "Scintillation in ground-to-space and retroreflected laser beams," *Opt. Eng.* **33**, 2535–2543 (1994).
4. L. C. Andrews, R. L. Phillips, and P. T. Yu, "Optical scintillations and fade statistics for a satellite-communication system," *Appl. Opt.* **34**, 7742–7751 (1995); "Optical scintillations and fade statistics for a satellite-communication system: Errata," *Appl. Opt.* **36**, 6068 (1997).
5. J. D. Shelton, "Turbulence-induced scintillation on Gaussian-beam waves: theoretical predictions and observations from a laser-illuminated satellite," *J. Opt. Soc. Am. A* **12**, 2172–2181 (1995).
6. M. S. Belen'kii, V. V. Boronoev, N. Ts. Gomboev, and V. L. Mironov, "Optical Sounding of Atmospheric Turbulence (Novosibirsk, Nauka, 1986) (in Russian).
7. A. P. Aleksandrov, G. M. Grechko, A. S. Gurvich, V. Kan, M. Kh. Manarov, A. I. Pakhomov, Yu. V. Romanenko, S. A. Savchenko, S. I. Serova, and V. G. Titov, "Spectra of temperature variations in the stratosphere as indicated by satellite-borne observation of the twinkling of stars," *Izv. Atmos. Ocean Phys.* **26**, 1–7 (1990).
8. F. Dalaudier, A. S. Gurvich, V. Kan, and C. Sidi, "Middle stratosphere temperature spectra observed with stellar scintillation and *in situ* techniques," *Adv. Space Res.* **14**, 61–64 (1994).
9. R. R. Beland, "Propagation through atmospheric optical turbulence," in *The Infrared and ElectroOptical Systems Handbook*, F. G. Smith, ed. (SPIE Optical Engineering Press, Bellingham, Wash., 1993), Vol. 2, Chap. 2.
10. M. G. Miller and P. L. Zieske, "Turbulence environmental characterization," RADC-TR-79-131, ADA072379, Rome Air Development Center (1979).
11. C. E. Coulman, J. Vernin, Y. Coqueugniot, and J. L. Caccia, "Outer scale of turbulence appropriate to modeling refractive-index structure profiles," *Appl. Opt.* **27**, 155–160 (1988).
12. V. I. Tatarskii and V. U. Zavorotny, "Atmospheric turbulence and the resolution limits of large ground-based telescopes: comment," *J. Opt. Soc. Am. A* **10**, 2410–2414 (1993).
13. W. W. Brown, M. C. Roggeman, T. J. Schultz, T. C. Havens, J. T. Beyer, and L. J. Otten, "Measurement and data-processing approach for estimating the spatial statistics of turbulence-induced index of refraction fluctuations in the upper atmosphere," *Appl. Opt.* **40**, 1863–1871 (2001).
14. J. T. Beyer, M. C. Roggeman, L. J. Otten, T. J. Schultz, T. C. Havens, and W. W. Brown, "Experimental estimation of the spatial statistics of

- turbulence-induced index of refraction fluctuations in the upper atmosphere,” *Appl. Opt.* **42**, 908–921 (2003).
15. D. L. Fried, “Scintillation of a ground-to-space laser illuminator,” *J. Opt. Soc. Am.* **57**, 980–983 (1967).
 16. P. O. Minott, “Scintillation in an earth-to-space propagation path,” *J. Opt. Soc. Am.* **62**, 885–888 (1972).
 17. P. J. Titterton, “Scintillation and transmitter-aperture averaging over vertical paths,” *J. Opt. Soc. Am.* **63**, 439–444 (1972).
 18. J. L. Bufton, R. S. Iyler, and L. S. Taylor, “Scintillation statistics caused by atmospheric turbulence and speckle in satellite laser ranging,” *Appl. Opt.* **16**, 2408–2413 (1977).
 19. J. L. Bufton, “Scintillation statistics measured in an earth-space-earth retro-reflected link,” *Appl. Opt.* **16**, 2654–2660 (1977).
 20. H. T. Yura and W. G. McKinley, “Optical scintillation statistics for IR ground-to-space laser communication systems,” *Appl. Opt.* **22**, 3353–3358 (1983).
 21. R. K. Tyson, “Adaptive optics and ground-to-space laser communications,” *Appl. Opt.* **35**, 3640–3646 (1996).
 22. F. Dios, J. A. Rubio, A. Rodríguez, and A. Comerón, “Scintillation and beam wander analysis in an optical ground-satellite uplink,” *Appl. Opt.* **43**, 3866–3873 (2004).
 23. G. J. Baker and R. S. Benson, “Gaussian beam scintillation on ground to space paths: the importance of beam wander,” *SPIE Proc.* **5550**, 225–235 (2004).
 24. L. C. Andrews and W. B. Miller, “Single-pass and double-pass propagation through complex paraxial optical systems,” *J. Opt. Soc. Am. A* **12**, 137–150 (1995); “Single-pass and double-pass propagation through complex paraxial optical systems: Errata,” *J. Opt. Soc. Am. A* **12**, 2213 (1995).
 25. A. S. Gurvich and M. S. Belen’kii, “Influence of stratospheric turbulence on infrared imaging,” *J. Opt. Soc. Am. A* **12**, 2517–2522 (1995).
 26. M. S. Belen’kii, S. J. Keris, J. M. Brown, and R. Q. Fugate, “Measurements of tilt anisoplanatism,” *Proc. SPIE* **3126**, 481–487 (1997).
 27. G. C. Valley, “Isoplanatic degradation of tilt correction and short-term imaging systems,” *Appl. Opt.* **19**, 574–577 (1980).
 28. D. L. Fried, “Anisoplanatism in adaptive optics,” *J. Opt. Soc. Am.* **72**, 52–61 (1982).
 29. B. M. Welsh and C. S. Gardner, “Effects of turbulence-induced anisoplanatism on the imaging performance of adaptive-astronomical telescopes using laser guide stars,” *J. Opt. Soc. Am. A* **8**, 69–80 (1991).
 30. R. J. Sasiela, “Strehl ratios with various types of anisoplanatism,” *J. Opt. Soc. Am. A* **9**, 1398–1402 (1992).
 31. A. M. Prokhorov, F. V. Bunkin, K. S. Gochelashvily, and V. I. Shishov, “Laser irradiance propagation in turbulent media,” *Proc. IEEE* **63**, 790–809 (1975).
 32. L. C. Andrews, R. L. Phillips, and C. Y. Hopen, “Scintillation model for a satellite communication link at large zenith angles,” *Opt. Eng.* **39**, 3272–3280 (2000).
 33. L. C. Andrews, R. L. Phillips, and C. Y. Hopen, *Laser Beam Scintillation with Applications* (SPIE Press, Bellingham, Wash., 2001).

34. M. A. Al-Habash, L. C. Andrews, and R. L. Phillips, "Mathematical model for the irradiance PDF of a laser beam propagating through turbulent media," *Opt. Eng.* **40**, 1554–1562 (2001).
35. P. Gatt, T. P. Costello, D. A. Heimmermann, D. C. Castellanos, A. R. Weeks, and C. M. Stickley, "Coherent optical array receivers for the mitigation of atmospheric turbulence and speckle effects," *Appl. Opt.* **35**, 5999–6009 (1996).